University of Wisconsin Milwaukee

UWM Digital Commons

May 2019

Investigation of Performance and Cavitation Treatment in a Kaplan Hydro Turbine

Muhannad R. Al-Haddad
University of Wisconsin-Milwaukee

INVESTIGATION OF PERFORMANCE AND CAVITATION TREATMENT IN A KAPLAN HYDRO TURBINE

by

Muhannad Al-Haddad

A Thesis Submitted in

Partial Fulfillment of the

Requirements for the Degree of

Master of Science

in Engineering

at

The University of Wisconsin-Milwaukee

May 2019

ABSTRACT

INVESTIGATION OF PERFORMANCE AND CAVITATION
TREATMENT IN A KAPLAN HYDRO TURBINE

by

Muhannad Al-Haddad

The University of Wisconsin-Milwaukee, 2019
Under the Supervision of Professor Ryoichi Amano

Cavitation is a phenomenon that occurs in various turbomachinery applications causing drawbacks on the. Some of these downsides are damaging the components of the system, generating noise and vibration, and loss of the turbine efficiency over time. Thus, it is imperative to address issue of cavitation to increase the life span of the equipment in addition to improve the system performance. This thesis introduces a method used to mitigate the cavitation phenomenon in a 3-inch Kaplan hydro turbine via injecting air at the leading edge of the rotor blades. The study is based on modeling the turbine using Computational Fluid Dynamics (CFD) software as well as carrying out experimental tests. The simulations were conducted at different air injection pressures over a spectrum of rotational speeds using Large Eddy Simulation (LES) for turbulence and volume of fluid for multiphase interactions: water, vapor water and air. The cavitation behavior was observed first without aeration, then followed by air injection simulations to investigate the effect of aeration. Each case was simulated for 12 cycles at rotational speeds of 1000, 2000, 3000, 4000, and 5000 rpm. The Vapor Volume Fraction (VVF) and the output mechanical power were monitored throughout the simulations. The data acquired from the simulations were compared to the experimental results for verifications. It was observed that the cavitation was mitigated in both the computer simulations and the experiment testing reaching up to 49.7% as an average reduction, while the output power was reduced by 6.6%.

TABLE OF CONTENTS

LIST OF FIGURES

LIST OF TABLES

LIST OF SYMBOLS

C	Convective Courant Number
C_w	Model coefficient
D	Diameter
ft	Feet
G	Rate of vapor generation
g	Gravitational acceleration $(\mathrm{m/s^2})$
g_{ij}	$= \frac{\partial \langle u_i \rangle}{\partial x_j}$, Velocity gradient tensor
I	Identity matrix
k	Turbulent kinetic energy
k_{SGS}	SGS turbulent kinetic energy
l	Order of phase
l	Distance between the center of the curved guide vane and the center of pipe
L	Moment on the turbine $(\mathrm{m \cdot N})$
L	$= {}^r/r_0$, Dimensionless number
m	Meter
N	Rotational Speed (rpm)
p	pressure
P_s	Surrounding liquid pressure
P_V	Vapor pressure
P_∞	Upstream pressure
psi	Pound per inch
psig	Pound per inch gauge
Q	Mass flow rate of water (kg/s)
R	Bubble radius
R_{ij}	Reynolds stress term

R_{shaft}	Radius of the shaft
S_{ij}	Strain rate tensor
S_{α_i}	source or sink of the ith phase.
t	Time
T	Temperature
u	Velocity
u_τ	Friction velocity
U_∞	Reference velocity
$U(\emptyset)$	Uncertainty of $\emptyset$
V	Flow average velocity magnitude
x_i	Physical coordinate system
$\tilde{x}$	Spatial cut-off value
W	Power output (W)
y	Wall distance
Y^+	$= \frac{u_\tau y}{\nu}$, normalized wall distance
z	Fluid height
$\forall_c$	Control volume
$\forall_i$	Volume of the ith phase in a control volume
$\langle \rangle$	Filtering operator
$\sim$	SGS components

GREEK LETTERS

α	Fraction function
α_i	ith phase volume fraction
δ_{ij}	Kronecker delta
Δ	Length scale
Δt	Time step size
θ	Angle (degree)
μ	Global phase dynamic viscosity
μ_t	Turbulent eddy dynamic viscosity
ν	Kinematic viscosity
ν_L	Liquid phase kinematic viscosity
ρ	Density
ρ_i	Density of the ith phase
ρ_L	Liquid density
ϕ	Fluid or flow property
σ	Cavitation number
σ_i	Inception cavitation number
$\overline{\sigma}_{ij}$	Molecular viscous stress tensor
τ_{ij}	Subgrid scale tensor
φ	Source/sink term
$\forall$	Volume

LIST OF ABBREVIATIONS

A.I.   Air Injection

CFD   Computational Fluid Dynamics

CFL   Courant-Friederichs-Lewy

DC   Direct Current

GS   Grid Scale

LES   Large Eddy Simulation

N-S   Navier-Stokes

Re   Reynolds number

rpm   Revolutions per minute

SGS   Sub Grid Scale

VDC   Volts Direct Current

VOF   Volume Of Fluid

VSD   Variable Speed Drive

VVF   Vapor Volume Fraction

ACKNOWLEDGEMENTS

First, I would like to thank my advisor, **Professor Ryo Amano**, for his continuous guidance in preparing this thesis. His support and input have enriched the content of this research and steered it to the right direction to present it at its current form. His previous work and research on hydro turbines and CFD, had influenced me in formulating this study.

Also, I would like to express my appreciation and gratitude to the defense committee **Prof. John Reisel** and **Prof. Istavn Lauko** for their efforts and time in reviewing this work. Their feedback had enhanced the content and the formatting of the thesis work.

I also extend my gratitude to my colleagues in the Hydro Turbine Lab at the University of Wisconsin-Milwaukee and wish them all the best in their future endeavors. Special thanks to Ph.D. candidate **Tarek ElGammal** for his great assistance in developing the CFD models, and Ph.D. candidates **Ahmad Abbas, Mohammad Qandil,** and **Ahmad Abdel Hadi** for their help in the testing and running of the experimental work. Additionally, I would like to thank the great undergraduate team who helped in building the experimental setup and making the dream come true: **Caleb Rozema**, thank you for all the CAD work and realization of the air injection turbine design, **Nicholas DiPasquale** the Godfather of the experimental setup, **Cody Casper** for the image processing, and **Benjamin Sveum** for developing the air injection design.

Finally, and mostly, I would like to thank my parents and siblings for their continuous support, encouragement, and unconditional love. To my mother, thank you for all the motivation and sacrifices you have made to make me what I am. Without you all, I would not have been able to achieve this milestone in my life!

1. Introduction

1.1   Hydropower

The scarcity of fossil fuels and their environmental impact had led to increase the dependency on alternative energy resources worldwide. Renewable energies are among these alternative sources in which arising as possible substitutes to the conventional energy generation. However, renewable energies are considered expensive and have less efficiency compared to conventional resources. Thus, recent studies in the energy field are focused on enhancing the efficiency of harnessing renewable energy and improving the quality of the power generated to make them more feasible and to be considered the sole candidates for all future power plants.

In 2016, renewable energies in their various forms accounted for 18.2% of the total energy consumption worldwide [1]. Hydropower had the highest share among the other renewable energy sources of the aforementioned percentage with 71% [2]. The leading countries in the hydropower generation are China, Canada, Brazil and U.S.A. as shown in Figure 1. In the United States, hydropower generated 7.5% of the total electricity in 2017 with an estimate of 300 billion kWh placing it as third energy source after fossil fuels (gas and coal) and nuclear preceding other renewable sources [3].
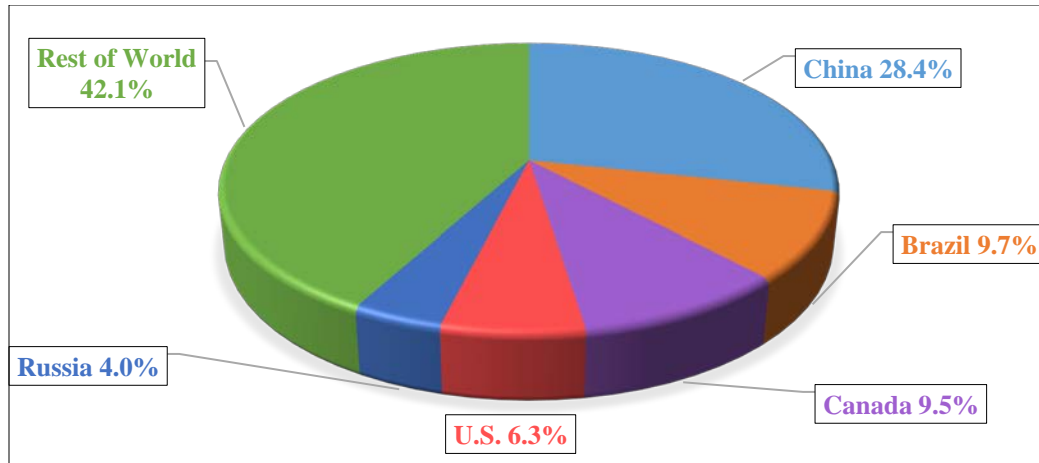
Figure 1: Percentage of annual hydropower production per country [4]

Hydropower is the energy generated via the forces in flowing water such as in rivers, streams and dams as well as tidal waves in oceans. It is considered one of the oldest sources of energy used to produce mechanical and electrical energy and was used to grind grains using paddle wheels. The amount of the available energy is dependent on the elevation difference in addition to the volume of water flowing. The energy is extracted using a turbine connected to an electrical generator that transform the rotational energy to electricity. As of today, the largest hydroelectric plant is the Three Gorges Dam in China with a generating capacity of 22.5 GW while the largest plant in the U.S. is the Grand Coulee Dam with 6.809 GW generating capacity [5, 6].

Hydro turbines are classified into two main categories depending on the action of water on the blades: reaction and impulse. In the reaction turbines, such as Francis and Kaplan (propeller), a pressure casing encompasses the blades which are fully immersed in water and the blades are angled to lift forces through the pressure differences. The runner in the impulse turbines, such as Pelton, operates in air and the rotational movement is created by one or more jets of water impinging on the blades. Reaction turbines are most common in low to medium-head applications whereas impulse turbines are used in high-head applications. Figure 2 illustrates the head and flow rate ranges for the different types of turbines.
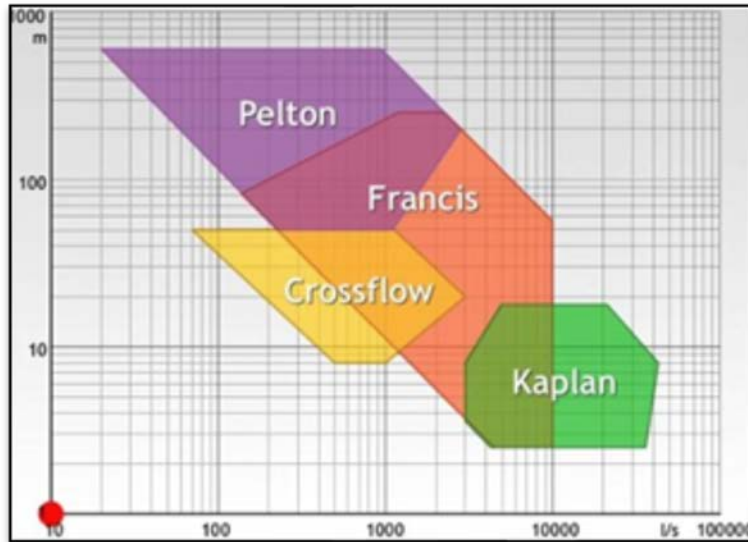
Figure 2: Head and flow ranges of hydro turbine types [7]

1.2   Cavitation Phenomenon Description

Cavitation is a phenomenon of the liquid to vapor transformation due to a sudden drop in pressure at a constant temperature. It occurs when the pressure falls below the vapor pressure of the liquid causing the transformation to vapor and thus formation of bubbles. Although cavitation and boiling may seem similar since both represent a liquid to gas phase change, however, the approach and the conditions of the phase transformation is different. Heating is the driving force of the phase change in boiling phenomenon in which as the molecules are being superheated, they gain kinetic energy causing rupture of the liquid. Whereas, cavitation occurs due to a drop in the pressure at a roughly constant temperature breaking the tensile forces between the molecules and leading to liquid rupture. The difference between two processes can be inferred from Figure 3. Boiling is represented by the constant pressure horizontal line, while cavitation is represented by the constant temperature vertical line.

3
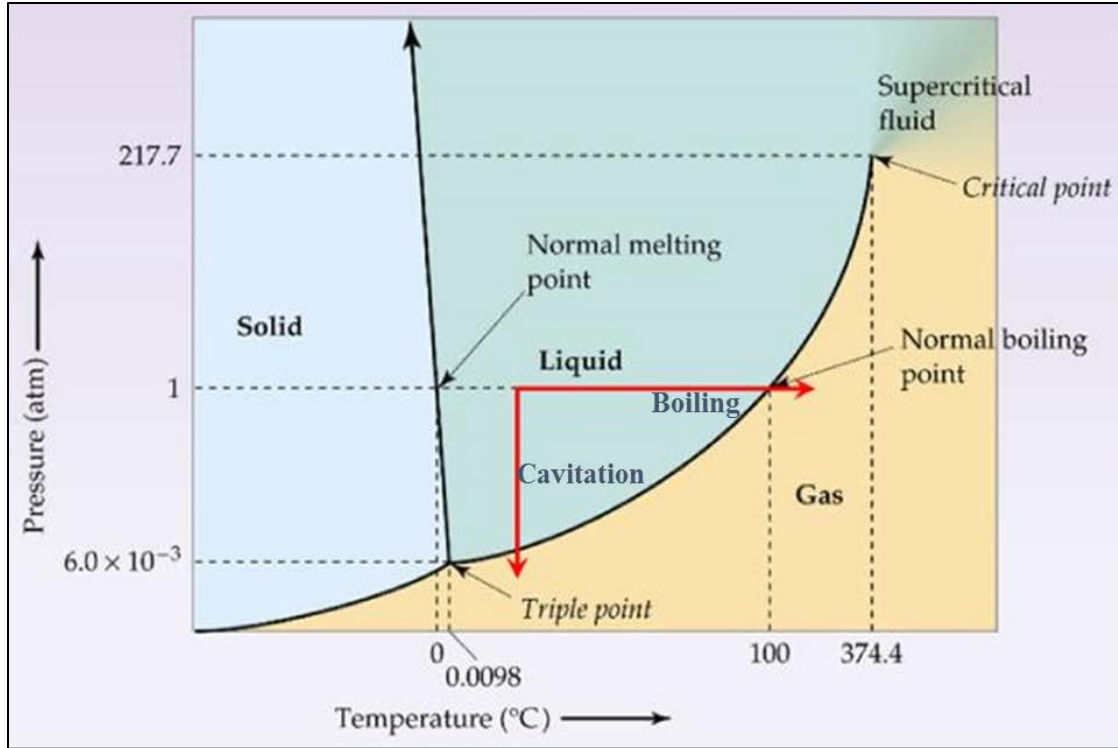
Figure 3: Phase change on pressure-temperature diagram [8]

To characterize if the flow has the potential to cavitate, a dimensionless number is defined. Cavitation number is used to express the possibility of the flow to cavitate at a certain condition. It relates the pressure of a flowing stream to the liquid vapor pressure at that certain condition. The cavitation number is extracted from the Bernoulli's equation:

$$P_1 + \frac{1}{2}\rho V_1^2 + Z_1 = P_2 + \frac{1}{2}\rho V_2^2 + Z_2 \qquad (1)$$

With a negligible height difference, the correlation becomes:

$$\sigma = \frac{P_\infty - P_v}{\frac{1}{2}\rho_L V_\infty^2} \qquad (2)$$

Where σ is the cavitation number. The lower the cavitation number the higher the possibility of cavitation to occur.

4

Cavitation has been associated with some adverse in turbomachinery applications including the most common problem: material damage. Due to the collapse of the bubbles nearby a solid surface, severe damage can occur to the runner, blades, impellers and parts within the system. The collapse of the cavitation bubbles is a fierce process that creates localized large-amplitude shock waves and microjets in the fluid where the collapse occurs causing stresses on the adjacent solid surfaces [9]. Having the cavitation bubbles collapse repeated leads to fatigue failure, pitting and eventually pieces of materials detachment. Figure 4 and 5 represent examples of localized damage on a pump blade due to cavitation.

Figure 4: Localized cavitation damage on a pump blade [9]

Figure 5: Severe cavitation erosion as witnessed on a Francis turbine [10]

Additionally, cavitation generates noise and vibrations which affects the stability and system performance. The high pressures that are caused momentary when the bubbles are compressed and collapsed result in noise and vibrations. Moreover, vibrations can initiate cracks especially in low-head turbines applications such as Kaplan turbines [9]. It occurs once the excitation frequency of the vortices coincides with one of the natural frequencies within the system leading to cracks in the turbomachinery components.

Large-scale cavitation structures can be classified into three main types: vortex, sheet and cloud cavitation. Vortex cavitation can be recognized by the cavitation formed in the vortex core where the pressure is smaller significantly than the other regions in the flow domain. Vortices usually form in flows with a high Reynolds number such as pump impellers and swirling flow in the draft tube of a hydro turbine. Tip vortex cavitation is a form of cavitation that occurs when bubbles are trapped in the center of the vortex that formed on the tip of a hydrofoil which is the low-pressure region [11]. Further reduction of the cavitation number will induce filling the vortex core with vapor. An example of a tip vortex cavitation is shown in Figure 6.

Figure 6: Tip vortex cavitation as witnessed on a Kaplan runner [12]

Cloud cavitation is a periodic formation and collapse of multiple cavitation bubbles in the form of a cloud. It occurs due to the scattering of cavitating vortices and a result of a periodic disturbance imposed on the flow. The cloud cavitation can be observed in the interaction between the stator and rotor of pumps and hydro turbines as well as in ships propellers and the wake region. The collapse of the cloud cavitation is proved to cause more noise and a higher potential for damage than flows with no fluctuations [13, 14]. Figure 7 shows a cloud cavitation formation on the suction side of a hydrofoil.
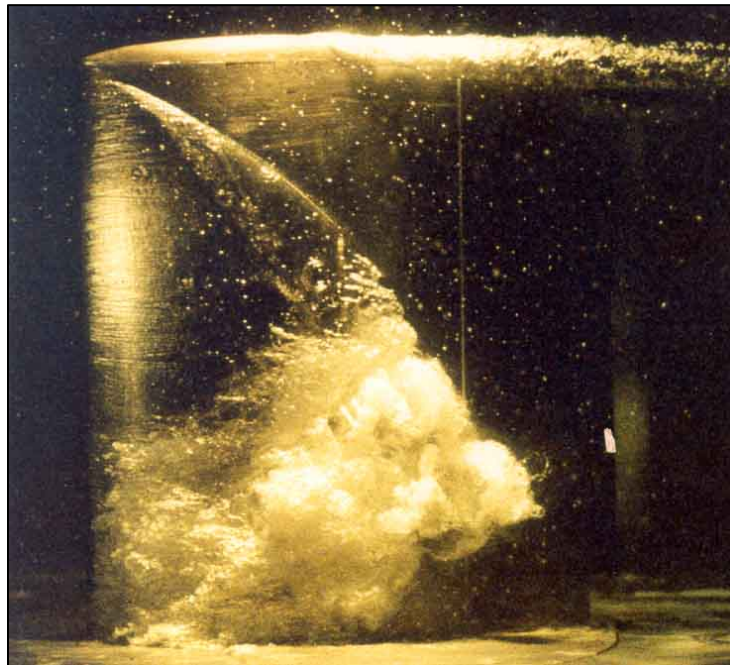
Figure 7: Cavitation cloud as seen on the suction side of a hydrofoil [15]

Sheet cavitation occurs when a region of separated flow is transformed into vapor and a "sheet" like zone is formed. It is observed as a vapor-filled separation zone or wake that is often called fully developed or attached cavity. On a hydrofoil or a propeller blade it is called sheet cavitation, whereas in pumps known as blade cavitation. An example of sheet cavitation is exhibited in Figure 8.
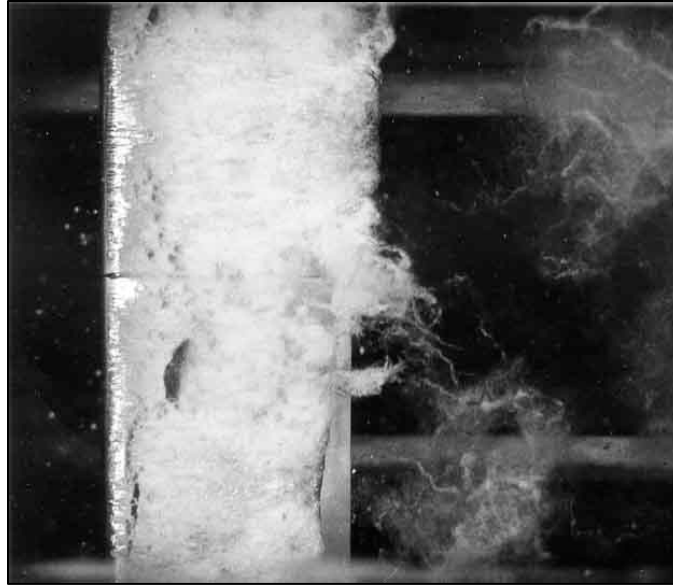
Figure 8: Sheet cavitation observed on the suction side of a hydrofoil [16]

1.3   Previous Studies

Many studies, including experimental and theoretical, were conducted to model and analyze cavitation, investigate the effects of cavitation, and find solutions to reduce the impact of cavitation. Different opinions were introduced discussing the effects of cavitation and reasons behind the performance declination as well as ways to overcome these drawbacks. However, most studies inferred that cavitation has an adverse effect on the performance of the hydro turbine systems.

Theoretical investigations showed that cavitation is one of the main causes of damage in Kaplan and Francis hydro turbines in addition to material defects and fatigue [17]. Through improving the design parameters and production of the turbines, the erosion induced by cavitation has been reduced. Another study concluded that cavitation causes pitting and identified typical locations of cavitation pitting as well as ways to repair the pitting [18].

8

Some experimental investigations were carried out to detect cavitation based on analyzing the vibration and acoustic diagnosis. Escalera et al. [19] evaluated the detection of cavitation through analyzing vibrations and acoustics. The study indicated that various cavitation patterns can be found at different parts of the hydro turbine. Bajic [20] utilized signal processing, noise analysis and data processing in the diagnosis and interpretation of cavitation in hydro turbine applications. The research led to modeling the cavitation intensity through extracting data from the experimental work that was carried out.

Additionally, Grekula and Bark [21] studied the mechanism of the erosion caused by cavitation in a Kaplan turbine experimentally using high-speed filming. It was observed that a cavitating tip vortex is formed at the blade root and bending towards the blade forming a cloud. The cavitation cloud appeared in a periodic pattern in addition to erosion indication due to forming a fine-scale cloud near the blade surface.

Cavitation in Kaplan turbines often occurs in two forms: tip clearance and tip vortex cavitation [22]. Tip clearance cavitation takes place due to a high leakage flow in clearance and depends on the differential pressure between the suction and pressure sides of the blade. Tip vortex cavitation initiates at the leading edge of the blade detaching the blade suction side. Both types are believed to have a little dependency on the cavitation number.

Air introduction into a hydraulic system to mitigate the cavitation phenomenon is not a new technique. Although not commonly known, it is used to influence the cavitation behavior in an already cavitating flow by increasing the pressure in the system, thus reducing the potential of cavitation occurrence. Air injection can be introduced by the means of a compressed air where the cavitation in anticipated to take place; low static pressure regions e.g.: suction side of a hydrofoil or leading edge of a hydro turbine.

There are previous studies and research conducted to investigate the effect of air introduction. Ardent *et. al.* [23] investigated the use of air injection to alleviate the erosion caused by cavitation in a study to improve the hydropower generation in a utility provider. The experimental work was performed on a specially instrumented hydrofoil and a NACA 0015 cross section in a water tunnel and tested flows up to 20 m/s velocities. The vibration and cavitation noise were measured using an ASTM vibratory apparatus and hydrophone. Pitting rate was inferred through measuring the impulse pressure and air was injected at the leading edge of the hydrofoil. The air injection was found to be an effective technique in minimizing the cavitation erosion.

Zhi-yong *et. al.* [24] investigated the control of cavitation by aeration experimentally and theoretically at flow velocities 20-50 m/s. The pressure waveforms were measured with and without aeration and the variation of the compression ratios at different air concentration was identified. The experimental results indicated that with aeration the pressure was increased significantly in the region where cavitation is anticipated. Additionally, the compression ratio increased with increasing the air concentration.

Tomov *et. al.* [25] studied the effect of aeration on a transparent horizontal venture nozzle by injecting compressed air and capturing images using a high-speed camera. The study compared the experimental results of the aerated and non-aerated cavitation by image processing for three different regimes: sheet cavitation, cloud cavitation, and super-cavitation. The experimental study showed that the symmetrical cavitation structures were partially broken in the case of sheet cavitation and cloud cavitation, while were completely disappeared when the super-cavitation was achieved.

Rivetti *et. al.* [26] investigated the effect of air injection on the tip vortex cavitation in a Kaplan hydro turbine. The experiments were carried out using a 0.34m diameter turbine located vertically between an upper and lower tanks. Air was introduced through twenty 3-mm-diameter holes located on a horizontal plane above the runner centerline. The data gathered through accelerometers, hydrophone, and high-speed camera were analyzed. Although the turbine efficiency was slightly reduced, however, air injection helped in alleviating the erosion caused by the tip vortex cavitation and the reduced the vibration in the whole system.

From all the above, it can be concluded that cavitation has a major impact on turbomachinery applications in which deteriorating the system performance and lifetime. Also, it limits the performance of hydro turbines due to the constraint of running at high rotational speeds. Thus, it is vital to address cavitation and introduce methods to alleviate the adverse caused by this phenomenon to improve the overall system performance and extend the lifespan of the turbomachinery components.

2. Methodology

2.1 Research Outline

The main objective of this research is to investigate the effect of air injection on the cavitation treatment and power generation in a Kaplan hydro turbine. Air is being introduced to the system through the turbine hub and is injected at the suction side of each blade. Numerical and experimental approaches were performed to identify the aeration effect as well as compare and validate the results. The numerical approach is performed first, using CFD, to optimize the design of the turbine and the air injection technique. Five simulations within each batch were completed to provide a range of different rotational speeds including 1000, 2000, 3000, 4000, and 5000 rpm. The experimental setup was built based on the CFD optimization and tested to validate the results.

The flow diagram of the work conducted in this research is shown in Figure 9. First, an initial CFD simulations were executed having a constant inlet water pressure to determine the water inlet velocity of rotational speed case. The water inlet velocity obtained from the first batch is used as an initial condition in the second batch of simulations. Then, the five rotational speed cases were simulated without aeration to determine the vapor volume of fraction in the system and the generated power. After that, air was introduced in the simulations at different gauge pressures for each rotational speed case and the VVF as well as the power generated were monitored. The experimental work was proceeded afterwards, and the collected data were compared with the CFD simulations results.

In this study, CFD simulations were executed using STAR CCM+ [27], a commercial software developed by Siemens. Large Eddy Simulation (LES), Volume of Fluid (VOF), and Wall-Adapting Local-Eddy Vis models were used to solve the unsteady multiphase turbulent flow.

Initial CFD: constant pressure inlet simluations

Constant velocity inlet CFD simulations

Air injection CFD simulations

Experimental testing

Comparison and Validation
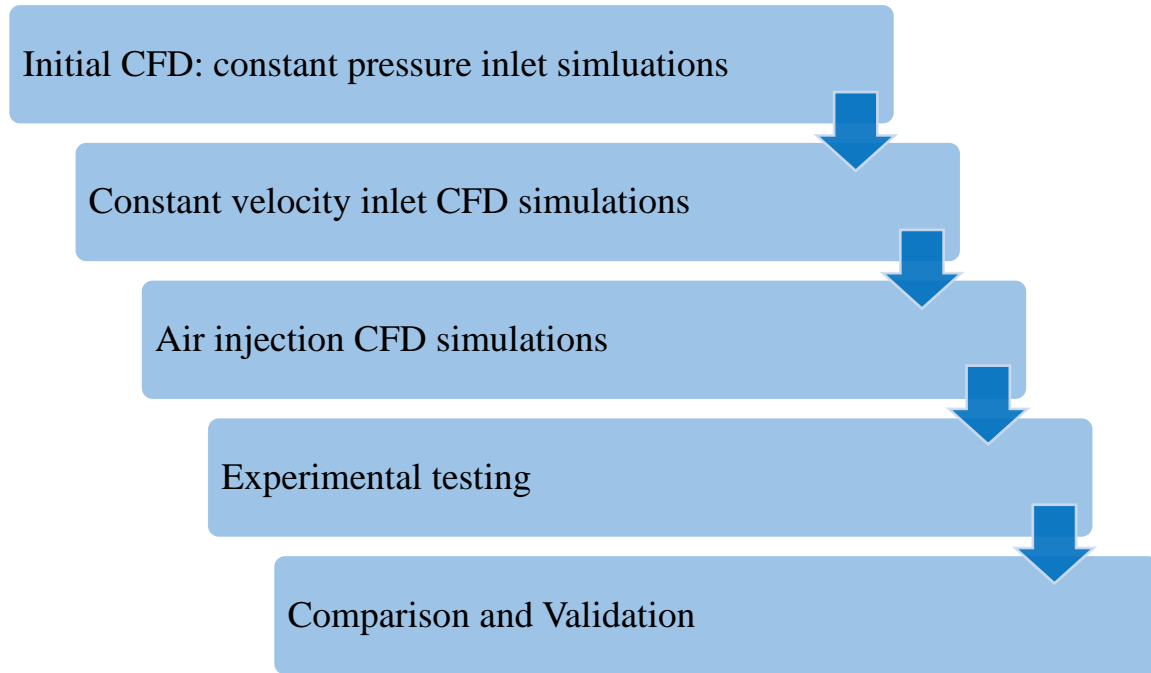
Figure 9: Flow diagram of research work

2.2   Computational Fluid Dynamics (CFD)

2.2.1 General

Computational Fluid Dynamics is a powerful numerical tool that is used to analyze fluid flow, heat transfer, and mass transfer systems. It is utilized for phase change, multi-phase, and chemical reactions cases to predict the pattern of flow, heat transfer, or mass transfer as well as solving complicated equations numerically. CFD can be employed to a wide range of applications such as turbomachinery, aircraft and vehicles aerodynamics, and metrology, as well as heating, ventilation and air-conditioning of buildings.

CFD has multi advantages over other analytical techniques and experimental approaches. It can be an effective cost and time saving approach to conduct a new design, investigate some research work or even for validation purposes. It can study a system that is complicated to perform experimentally and provide different scenarios without building a test rig. There are different commercial software that are capable of executing CFD simulations for various applications. However, they undergo a similar approach of solving the governing equations and processing the results to a user-friendly interface.

There are three different numerical solution methods: finite difference, finite element, and spectral methods [28]. These numerical solution methods are the basis of any CFD solver. The solvers perform: approximation of the unknown variables, discretization, and solution of algebraic equations.

2.2.2 Large Eddy Simulation (LES)

Turbulence flow is characterized by random eddy motion of different scales. Small-scale eddies require fine meshing to be resolved, however, fine meshing will increase the cost of numerical computation since it will require high processing computers and long time to accomplish. LES decomposes the turbulent flow into solvable Grid Scale (GS) eddies which are larger than the grid size, and modeled Sub Grid Scale (SGS) eddies as indicated in Equation (3). Therefore, LES can be utilized to overcome the problem of expensive computations.

$$\phi = \bar{\phi} + \phi' \tag{3}$$

LES filters the fluid/flow properties (ϕ) scales by using a filtration function $G(x - \hat{x}, t - \hat{t})$ allowing larger values than space and time cut-off limits ($\hat{x}, \hat{t}$), and weighing the property via a length scale (Δ) function. The operation and the filtering are shown in Eq. (4) and (5).

$$\overline{\phi(x,t)} = \int\limits_{-\infty}^{\infty}\!\!\!\int \phi(\hat{x},\hat{t})\, G(x-\tilde{x},t-\tilde{t})\, d\tilde{x}\, d\tilde{t} \tag{4}$$

$$(x) = \begin{cases} \dfrac{1}{\Delta} & \left(|x| < \dfrac{2}{\Delta}\right) \\[2mm] 0 & \left(|x| < \dfrac{2}{\Delta}\right) \end{cases} \tag{5}$$

The cavitation alters the nature of the VOF flow making the density a function of time and space. The LES solves the governing equations in the compressible state providing accurate treatment. The Favre filtering [29] applies to the LES when adding the density as a variable, leading to Eq. (6).

$$\tilde{\phi} = \frac{\overline{\rho\phi}}{\bar{\rho}} \tag{6}$$

The resultant continuity and N-S equations for the filtered field scale by Favre Filtration are expressed in a tensor form in Eqs. (7) and (8). Residual (or sub-grid scale) turbulent stress tensor (τ_{ij}) proposed by Leonard [30] related the complex filtered advection term $(\frac{\partial(\overline{\rho\, \widetilde{u_i u_j}})}{\partial x_j})$ to the multiplication of the filtered velocities $(\frac{\partial \bar{\rho}\tilde{u}_i\tilde{u}_j}{\partial x_j})$.

$$\frac{\partial \bar{\rho}}{\partial t} + \frac{\partial \bar{\rho}\tilde{u}_i}{\partial x_i} = 0 \tag{7}$$

$$\frac{\partial \bar{\rho}\tilde{u}_i}{\partial t} + \frac{\partial \bar{\rho}\tilde{u}_i\tilde{u}_j}{\partial x_j} = -\frac{\partial \bar{p}}{\partial x_i} + \frac{\partial}{\partial x_j}(\tau_{ij+}\bar{\sigma}_{ij}) \tag{8}$$

τ_{ij} and $\bar{\sigma}_{ij}$ in the Eq. (8) are defined by Eqs. (9) and (10) respectively.

$$\tau_{ij} = -\bar{\rho}(\widetilde{u_i u_j} - \tilde{u}_i\tilde{u}_j) \tag{9}$$

$$\bar{\sigma}_{ij} = \mu(\tilde{T})\left(-\frac{2}{3}\frac{\partial \tilde{u}_k}{\partial x_k} + \frac{\partial \tilde{u}_i}{\partial x_j} + \frac{\partial \tilde{u}_j}{\partial x_i}\right) \tag{10}$$

where the molecular viscosity, $\mu(\tilde{T})$, is based on the Favre-filtered static temperature $\tilde{T}$ [31].

15

By defining (τ_{ij}) using Boussinesq's hypothesis [32] of linking the turbulence stress to an artificial turbulent viscosity (μt) which needs an SGS model to identify. Equations (11) and (12) are outlining the formulation for τ_{ij} (general and descriptive forms) based on the strain rate tensor of the fluid flow ($S_{ij} = \frac{1}{2}(\frac{\partial \overline{u}_i}{\partial x_j} + \frac{\partial \overline{u}_j}{\partial x_i})$) and SGS kinetic energy (K_{SGS})

$$\tau_{ij} = -\overline{\rho}(\widetilde{u_i u_j} - \tilde{u}_i \tilde{u}_j) \tag{11}$$

$$\tau_{ij} = 2\mu_t S_{ij} - \frac{2}{3}(\mu_t \nabla \cdot \vec{u} + \rho K_{SGS})I \tag{12}$$

With WALE model, μ_t is defined in terms of the length scale which is usually set at the half of $(\forall_c)^{\frac{1}{3}}$ near the wall, and the deformation parameter which is a non-linear function consisting of the gradients of the filtered velocities as the building unit [33], [34].

2.2.3 WALE Subgrid Scale Model

The WALE (Wall-Adapting Local-Eddy Viscosity) Subgrid Scale is an eddy viscosity model in which the length scale is filtered width (Δ) [35]. In WALE model, the SGS eddy viscosity ν_{SGS} is defined by using the filter width (Δ):

$$\nu_{SGS} = C_w \Delta^2 \frac{\left(S_{ij}^d S_{ij}^d\right)^{3/2}}{\left(S_{ij}^d S_{ij}^d\right)^{5/4} + \left(S_{ij} S_{ij}\right)^{5/2}} \tag{13}$$

, where the strain rate tensor S_{ij}, g_{ij} and the tensor S_{ij}^d are respectively defined as following;

$$S_{ij} = \frac{1}{2}\left(\frac{\partial \langle u_i \rangle}{\partial x_j} + \frac{\partial \langle u_j \rangle}{\partial x_i}\right) \tag{14}$$

$$g_{ij} = \frac{\partial \langle u_i \rangle}{\partial x_j} \tag{15}$$

$$S_{ij}^d = \frac{1}{2}\left(g_{ij}^2 + g_{ji}^2\right) - \frac{\delta_{ij}}{3}g_{kk}^2 , \qquad g_{ij}^2 = g_{ik}\, g_{kj} \tag{16}$$

16

2.2.4 Volume of Fluid (VOF)

VOF was introduced briefly in 1976 by Noh and Woodward [36] followed by a full method description by Hirt and Nichols in 1981 [37]. In such approach, the coexisted (n) fluids are accounted as a global one phase of fluid and flow properties calculated as an averaged sum based on the presence percentage of each phase in the computation cell by volume ratio $(\frac{\forall_l}{\forall_c})$. Accordingly, the ($l$)th phase volume fraction (α_l), and any equivalent property (ϕ) are calculated every time step as in Eqs. (17) and (18) respectively.

$$\alpha_l = \frac{\forall_l}{\forall_c} \tag{17}$$

$$\phi = \sum_{l=1}^{n} \alpha_l \, \phi_l \tag{18}$$

Since the system is always conserved, the volume fractions of the phases are also maintained in balance by solving the transport equation (also known as continuity) of each volume fraction as shown in Eq. (19). The equation considers the phase motion relative to the reference frame motion ($u - u_{rf}$), interface update, and phase addition/reduction due to source/sink (φ_{α_l}) existence.

$$\frac{\partial}{\partial t} \int_{\forall} \alpha_l \, d\forall + \int_{A} \alpha_l \, (u - u_{rf}) \, dA = \int_{\forall} (\varphi_{\alpha_l} - \frac{\alpha_l}{\rho_l} \frac{D\rho_l}{Dt}) \, d\forall \tag{19}$$

In situations of rapid phase change, like in cavitation, the global density varies temporally and locally at a high rate, and the source/sink term dominates. Meanwhile, the unsteady term exhibits a similar behavior and becomes difficult to be solved by the segregated flow method. To bypass the computational challenge, Eq. (20) is a simplified but non-conservative equation is derived from Eq. (19).

$$\int_A \dot{\alpha}_l \, (u - u_{rf}) \, dA = \sum_l \int_\forall \dot{} (\varphi_{\alpha_l} - \frac{\alpha_l}{\rho_l} \frac{D\rho_l}{Dt}) \, d\forall \tag{20}$$

It's worth mentioning that in the case of cavitation, the R.H.S of Eq. (19) represents the mass transfer rate of the vapor depending on the status of generation ($P_v > P_s$) or collapse ($P_v < P_s$). The rate of vapor generation and collapse is expressed by Eqs. (21) and (22) respectively [38].

$$G = \frac{\rho_v \rho_L}{\rho} \alpha(1 - \alpha) \frac{3}{R} \sqrt{\frac{2}{3} \frac{(P_v - P_s)}{\rho_L}} \tag{21}$$

$$C = \frac{\rho_v \rho_L}{\rho} \alpha(1 - \alpha) \frac{3}{R} \sqrt{\frac{2}{3} \frac{(P_s - P_v)}{\rho_L}} \tag{22}$$

In a consecutive computational step, the motion of the global phase (i.e. mixture) is solved by the compressible-flow momentum differential equation with the consideration of the isothermal and Newtonian fluid conditions as expressed in Eq. (23).

$$\frac{d(\rho \vec{u})}{dt} + \nabla \cdot (\rho \vec{u} \, \vec{u}) = \rho \vec{g} - \nabla P + \nabla \cdot [\mu(\nabla \vec{u} + \nabla \vec{u}^T)] \tag{23}$$

Where $\vec{g}$ is affecting in negative y-direction.

2.3 Numerical Models

2.3.1 Numerical Model Inputs and Geometry

As mentioned in section 2.1, the CFD models conducted in this thesis research can be outlined as follows:

1. Initial simulations with a constant inlet water pressure as a boundary condition

2. Constant water inlet velocity simulations as a boundary condition without aeration

3. Constant water inlet velocity simulations with air injection at different pressures

4. Experimental setup – CFD validation simulations (Propeller case)

In all of the afore-mentioned simulations, Large Eddy Simulation turbulence model was utilized as well as WALE subgrid scale model. The simulations took into consideration the phase change of water into water vapor, and thus, Eulerian Multiphase and Cavitation models were enabled. VOF model is used to quantify the cavitation and compare the results of the Vapor Volume Fraction (VVF) among the different cases. VVF is one of the determining factors that are monitored throughout all the simulations and used to interpret and identify the effect of aeration on cavitation.

The Kaplan turbine in which is under investigation, was designed and developed by the Hydro Turbine Lab at the University of Wisconsin-Milwaukee. The turbine has a stator of 9 blades and a rotor of five blades. Figure 10 exhibits a 3-dimensional geometry scene of the turbine. Whereas, a side view of the turbine is shown in Figure 11.
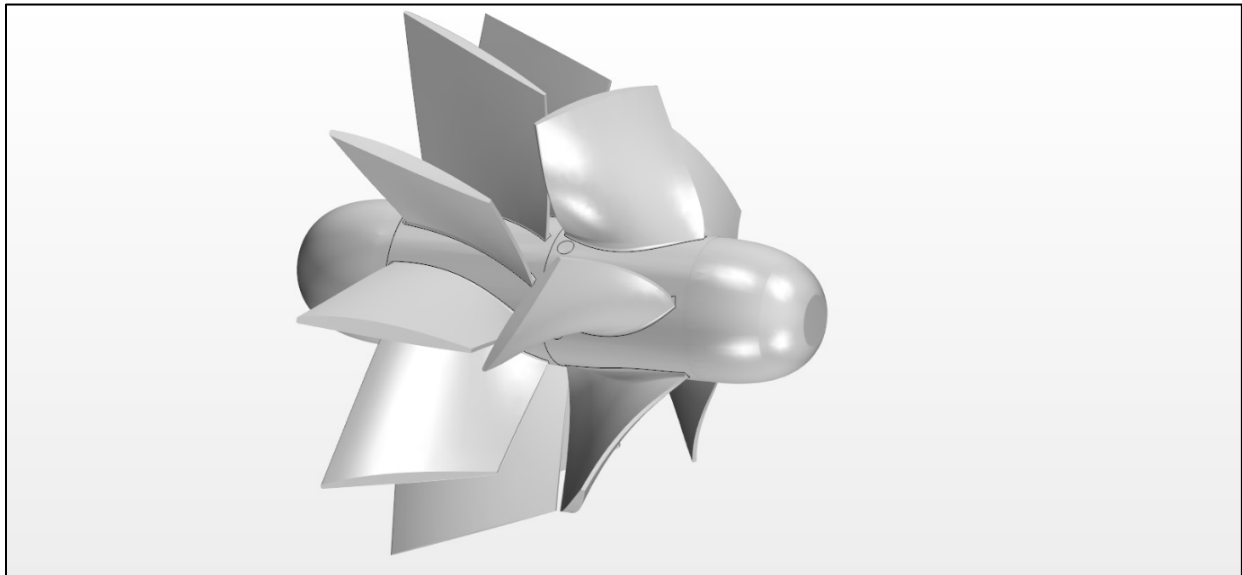
Figure 10: 3-D geometry view of the turbine
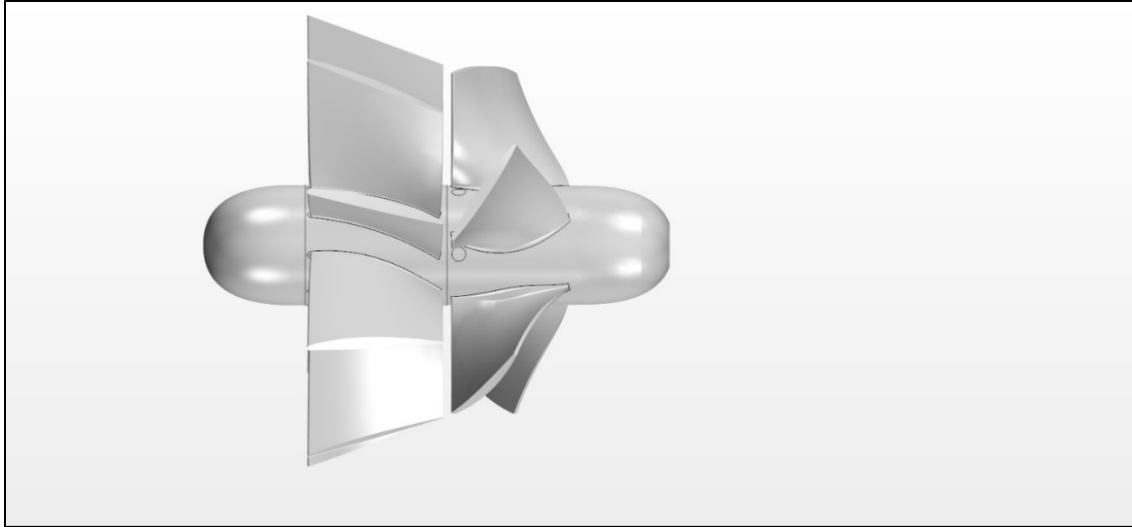
Figure 11: Side view of the turbine

The geometry of the numerical model as well as the simulation domain is indicated in Figure 12. The 3-inch (0.076 m) Kaplan turbine was simulated in a 6-inch (0.152 m) pipe having an inlet 6-inch to 3-inch reducer at the left-hand side and converted back to 6-inch. The diffuser at the right-hand side of the turbine has a length of 1.5 times the turbine diameter, 4.5 inches (0.114 m), and the length of the exit 6-inch pipe is 15 inches (0.381 m). The inlet boundary condition was set as a constant water pressure for the first batch of simulations and then changed to constant water velocity for the rest simulation cases. On the other side, the same outlet boundary condition was used in all simulation and set as an atmospheric pressure outlet, 101.3 kPa.
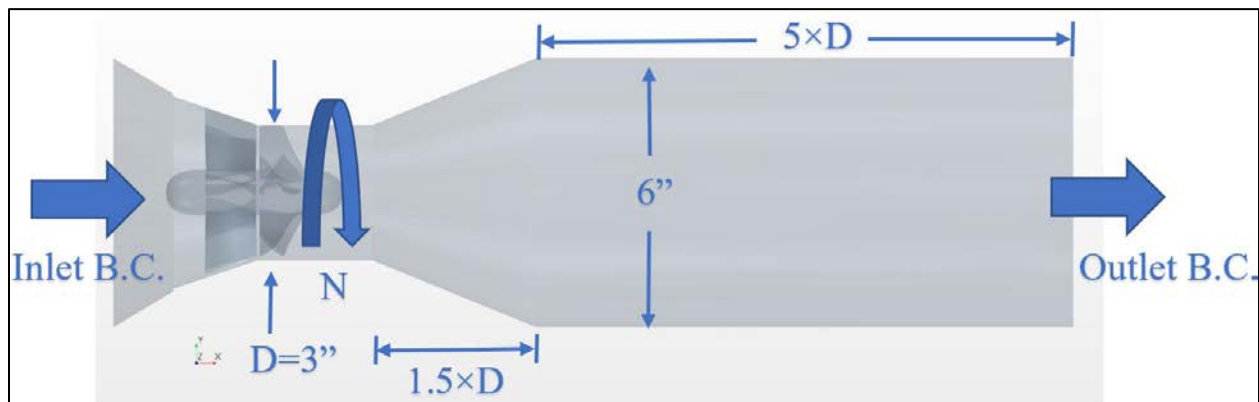
Figure 12: Geometry and domain of the numerical models

The turbine was set to rotate for twelve cycles per each simulation and the simulation stopping criteria was based on the maximum physical time for each rotational speed. The steady state condition was achieved after eight cycles. The results were based on a time averaged values for the last two cycles in each simulation.

The continua used in the numerical models included three fluid components and two phases: water, water vapor, air. The water vapor pressure was set as 3.17 kPa at temperature of 298 K.

2.3.2 Time Step

The time step is the incremental change in time for which the governing equations are being solved. It is advised to select small time-step size to capture all the flow fluctuations, however, the smaller the time step the longer the time is required to execute the simulation. Thus, it is imperative to optimize the time step without jeopardizing the accuracy of the results nor increasing the computation expenses.

There are some common approaches to optimize the time step in the numerical simulations. One approach is taking a percentage of the time scale which is the result of the division of the numerical domain length over the fluid velocity. In the rotational domain case, the optimum time step should be equal or less than one-degree rotation. The latter was utilized in this research and the time step was calculated based on the rotational speed. The time step and total time of each rotational speed are indicated in Table 1.

Table 1: Time step and total time per each rotational speed

Rotational Speed (rpm)	Time for One Complete Revolution (s)	Total Simulation Time for 12 Cycles (s)	Time Step (μs)
1000	0.06	0.72	100
2000	0.03	0.36	80
3000	0.02	0.24	60
4000	0.015	0.18	40
5000	0.012	0.144	30

Ten inner iterations were utilized for each time step in each simulation. Inner iterations are used to repeat the process of solving the governing equations numerically to achieve convergence. Therefore, the number of iterations can help to attain convergence, however, it the higher number of inner iterations the simulations will take longer time to be completed. Thus, optimization of the computational cost verses the accuracy of the solution must be considered.

2.3.3 Mesh Independent Study

Mesh size is also another significant factor that plays a role in achieving accuracy of the numerical solution. LES discretization error depends on the mesh size used in the simulation and affects the convergence of the solution. Fine meshing is also expensive computationally, but the solution validity should not be comprised. Thus, the grid size was studied prior to performing any simulations to ensure the optimization of meshing size throughout the mesh independent study.

Mesh independent study involves analyzing the solution of the simulations based on changing the discretization criteria of the computational domain only. The size of the cell is changed, and the solution time as well as the accuracy are monitored. Another way to analyze the mesh sizing is the Y^+ and the CFL numbers.

Y^+ is a dimensionless wall distance for a wall-bounded flow and known also as the Law of the Wall. It was introduced by Theodore von Karman in 1930 and is defined in Eq. (24). It is a function of the shear velocity near the wall, the distance to the nearest wall, and the kinematic viscosity of the fluid. Y^+ is used in turbulence models to indicate the effect of the influence of the Reynolds stress tensor [39]. The wall function approach is used to apply boundary conditions to a distance away from the wall, so the turbulence model equations are not solved close to the wall [40]. In simulation without wall functions, the value of Y^+ is usually around 1, and in simulations where wall functions are enabled the value of Y^+ is higher than 1. The viscous sublayer, which is a region within the boundary layer, has a value of $Y^+ < 5$.

$$Y^+ = \frac{u_\tau y}{\nu}$$

(24)

The Courant-Friedrichs-Lewy (CFL) is a conditional stability requirement that is dependent on the time step and the mesh spacing. It was introduced and discussed at length by Courant et al. in 1928 [41]. CFL condition states that the distance traveled by any information during the time step must be less than the distance between the mesh elements. The information is transferred from a cell and propagates to the immediate neighboring cells. The Courant number, or mean of Convective Courant number, is a dimensionless number that is a function of time step and the mesh size. It is defined in Eq. (25).

$$C = \frac{u \Delta t}{\Delta L}$$

(24)

Four grid sizes were studied for the simulation domain. The number of cells were 2.5, 3.5, 5.5 and 7.5 million cells. The meshing cell is unstructured polyhedral to capture the separation and wake regions in addition to other fluid interactions. Prism meshing was also utilized to capture the physics at the boundary layer with 8 layers at the stator and 12 layers at the rotor. The simulations were computed at 2000 rpm and without aeration and were conducted using 280 cores of a High-

Performance Computer (HPC). Table 2 indicates the VVF of each of each mesh size that was computed for the mesh independent study.

Table 2: Mesh independent test results

Number of Cells (in millions)	2.5	3.5	5.5	7.5
Mesh	Very coarse	Coarse	Fine	Very Fine
Blade Average VVF	0.0285	0.0273	0.0325	0.0321
Overall Average VVF	0.0301			

The blades VVF values of the cases indicated in Table 2 were averaged, and the averaged value was used in the selection of the grid size. The overall average VVF was used as a basis to calculate the deviation of the different cell size cases. Additionally, the computational time consumed for each case is monitored to investigate the impact of increasing the number of cells. The comparison of the VVF for the four number of cells simulations versus the overall averaged value as well as the computational time are shown in Table 3.

Table 3: Mesh independent test results

Number of Cells (in millions)	2.5	3.5	5.5	7.5
Percentage of VVF to overall Avg.	5.3%	9.3%	7.9%	6.7%
Computational Time (days)	1	1.5	2	3

Moreover, the wall Y^+ and the mean of Convective Courant numbers were monitored to choose the optimum cell size. The main criteria were based on having a wall Y^+ number close to 1 and a Courant number less than 5. The latter conditions were achieved in the 5.5 million cells meshing as shown in Figures 13 and 14 which are screenshots extracted from STAR CCM+. As it

can be inferred from both figures, the wall Y^+ number is less than 2, whereas, the Courant number is less than 5 according to Figure 14. Thus, and based on the results attained in Tables 2 and 3, the 5.5 million cells meshing was used since it provided an accuracy of results, stability, and within moderate computational time and cost.
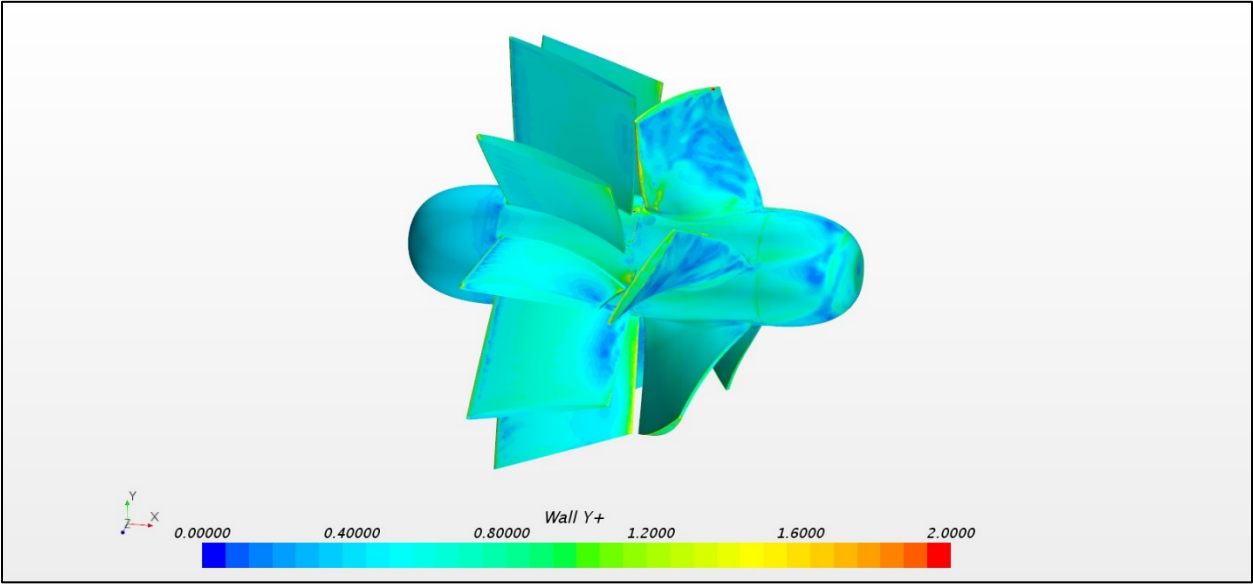
Figure 13: Wall Y^+ scene of the 5.5 million cells case
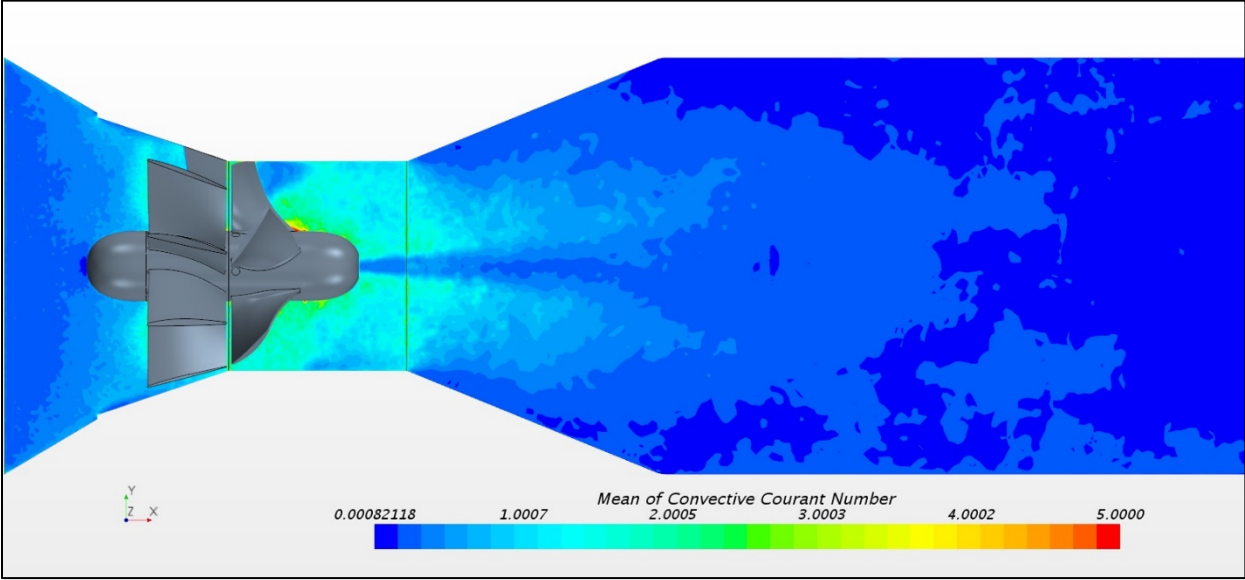
Figure 14: Mean of Convective Courant scene of the 5.5 million cells case

The mesh scene of the whole simulation domain is shown in Figure 15. As noticed from the figure, the cell size is not similar throughout the whole domain. The cells around the turbine are finer than the cells in the exit pipe. The reason behind this approach is to capture all the fluid interactions and the phase change of the water molecules at the rotational domain which is the region of interest of this research. Figure 16 exhibits a close scene of the grid cells around the turbine. The multiple lines that wrap the turbine's stator and rotor are the Prism layers.
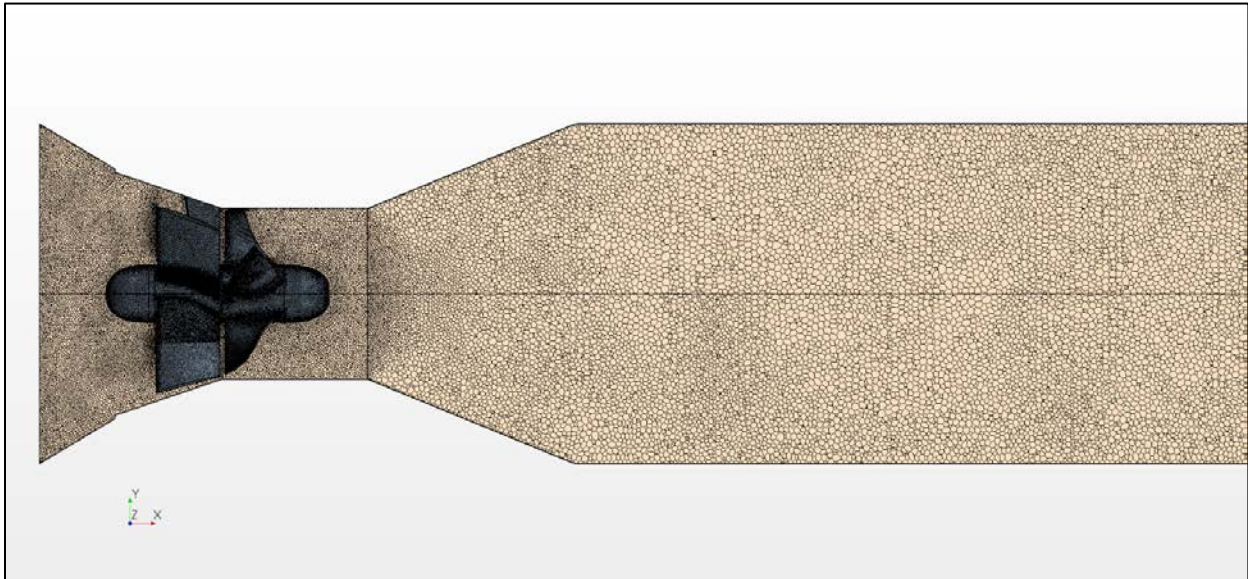
Figure 15: Mesh scene of the whole simulation domain
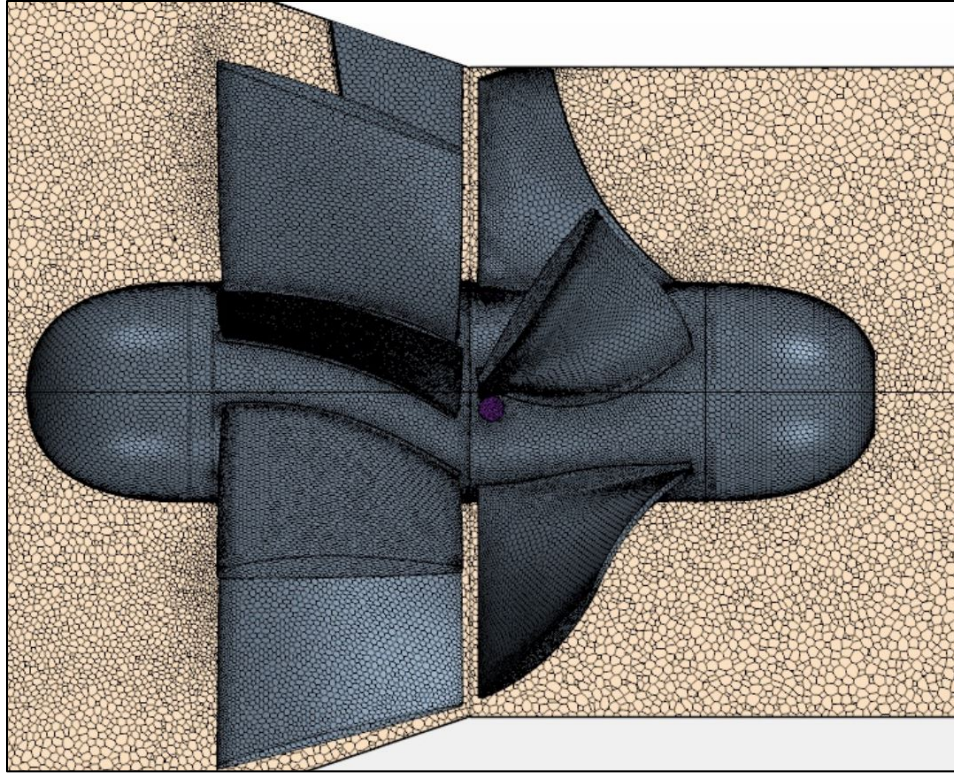
Figure 16: Mesh scene at the turbine region

2.4   Simulations without Aeration

2.4.1 Constant Pressure Inlet

As mentioned before, constant water pressure was set as an inlet boundary condition in the first run of simulations. The water pressure was set as 184.0 kPa (12 psig) ahead of the turbine and the outlet boundary condition. The main purpose is to obtain the water inlet velocities at different rotational speeds. This approach was sought to induce and guarantee the presence of cavitation prior air injection. It is useful when neither the mass flow rate nor the velocity of the fluid is known. Although using an inlet constant pressure as a boundary condition is not an erroneous method, however, velocity inlet is preferable for incompressible flows. Velocity inlet boundary condition results in a better convergence and hence enhanced stability. Table 4 represents the water

27

inlet velocities per each rotational speed after completing the water constant inlet pressure simulations.

Table 4: Water inlet velocity per each rotational speed

Rotational Speed (rpm)	Water Inlet Velocity (m/s)
1000	2.00
2000	2.15
3000	2.29
4000	2.45
5000	2.64

2.4.2 Constant Water Inlet Velocity

After obtaining the water velocities the inlet boundary conditions were changed, and velocity inlet were used instead of constant pressure inlet. The water velocities indicated in Table 4 for each rotational speed scenario were utilized as an inlet boundary condition along with water VOF of 1 and water vapor VOF as zero. The outlet boundary conditions were maintained as atmospheric pressure and similar VOF conditions as in the inlet. The simulations were executed and the VVF along with the absolute pressure and power generated were monitored.

It is also worth mentioning that the constant water inlet velocity boundary condition will ensure the study of aeration effect on the cavitation solely. The air injection will change the water velocity in constant inlet pressure case since the velocity is not set as a constant input in the simulations. Thus, the cavitation pattern will be affected due to the fluctuation in the water velocity. However, the water velocity will not be altered in the constant water inlet velocity case as the air is being introduced. Therefore, the cavitation pattern will only be affected by the air injection which is the aim of this research.

2.5   Air Injection Simulations

The air injection simulations are similar to the constant water velocity ones with the addition of aeration. Air is being introduced at the suction side of each blade near the leading edge as shown in Figure 17 with the magenta color. Each air injection port has a diameter of 3mm and a total of five ports distributed throughout the rotor. Air was injected at three different gauge pressures: 101.3 kPa (0 psig), 122.0 kPa (3 psig) and 135.8 kPa (5 psig) for each rotational speed leading to a total of 15 simulations with aeration. The cavitation patterns as well as the VFF were monitored and compared with the no aeration simulations. Additionally, the power generated per each simulation were compared with the no aeration case to investigate the effect of aeration on the turbine performance.
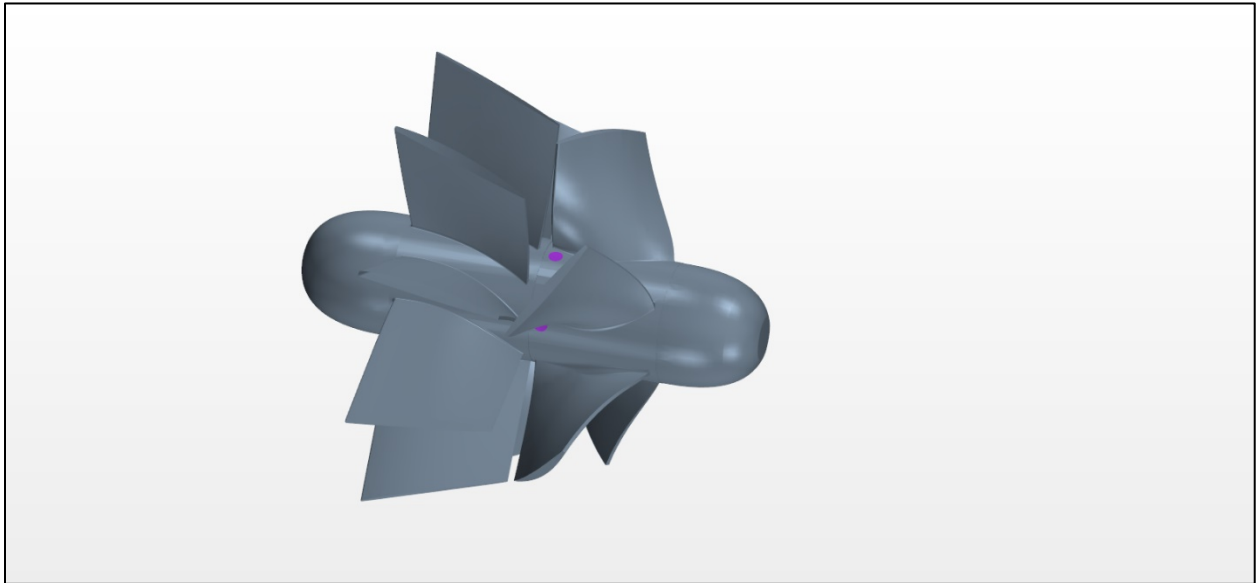

Figure 17: 3D geometry with air injection ports

3. Experimental Work

3.1   Setup Configuration

Experimentation helps in verifying the numerical computations and can be used as a tool to validate the results obtained from the CFD simulations. It demonstrates the accuracy of the CFD results and can be used to proceed with the simulations with confidence. Additionally, it determines the credibility of the programming and computational results as well as examines the models through comparison with the experimental results.

The experimental setup was built in the Hydro Turbine lab at the University of Wisconsin-Milwaukee hosting a relatively low-head Kaplan turbine. The system was designed to accommodate a horizonal turbine configuration with an elevated tank, a discharge reservoir, and a circulating pump, as shown in Figure 18. The setup is installed on a T-slot table that houses the lower tank providing supports to the hydro turbine system and adjustable configuration. The maximum head that can be achieved through this setup is 2.75m (9 ft). The upper tank has a capacity of 0.60 m³, Figure 19 (a), and the lower reservoir has a capacity of 0.45 m³. The 10 HP pump circulates the water between the two tanks and is equipped with a Variable Speed Drive (VSD) to control the pump flow rate during testing. The water flowing into the turbine is also controlled through a ball valve installed vertically on the 0.15 m (6 inches) down pipe as shown in Figure 19 (b).

Figure 18: Experimental setup

(a)

(b)

Figure 19: (a) Upper tank (b) Ball valve installed on the down pipe

The turbine housing is made of clear Acrylic, shown in Figure 20, that was casted on the university campus and consists of three sections:

1- Intake nozzle to convert the pipe diameter from 0.15 m (6") to 0.076 m (3")

2- Straight 0.076 m (3") section hosting the turbine rotor

3- Outlet diffuser changing the diameter back to 0.15 m (6")
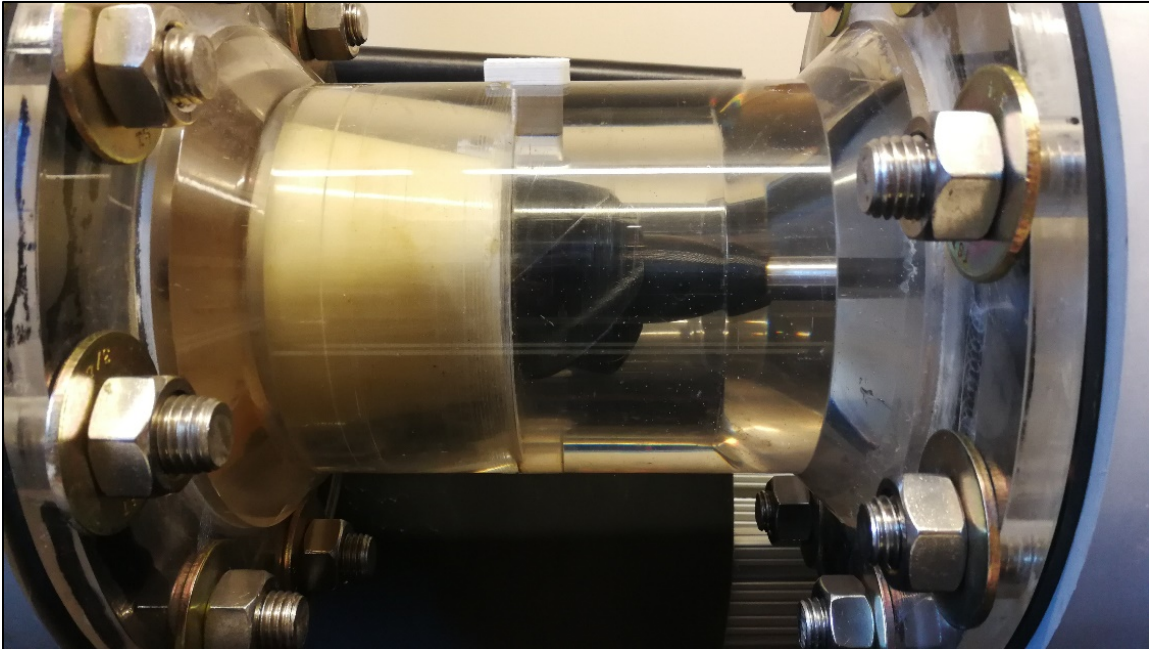
Figure 20: Turbine clear housing

The turbine is attached to a stainless-steel shaft of 0.016m (5/8") diameter that is connected a Magtrol torque-meter using non-slip coupling. The other side of the torque-meter is attached to a 2.25 HP DC permeant magnet motor that can be used as a generator through rewiring. The assembly of the shaft, torque-meter, and the motor is indicated in Figure 21. The electric power is dissipated through a resistive load-bank.
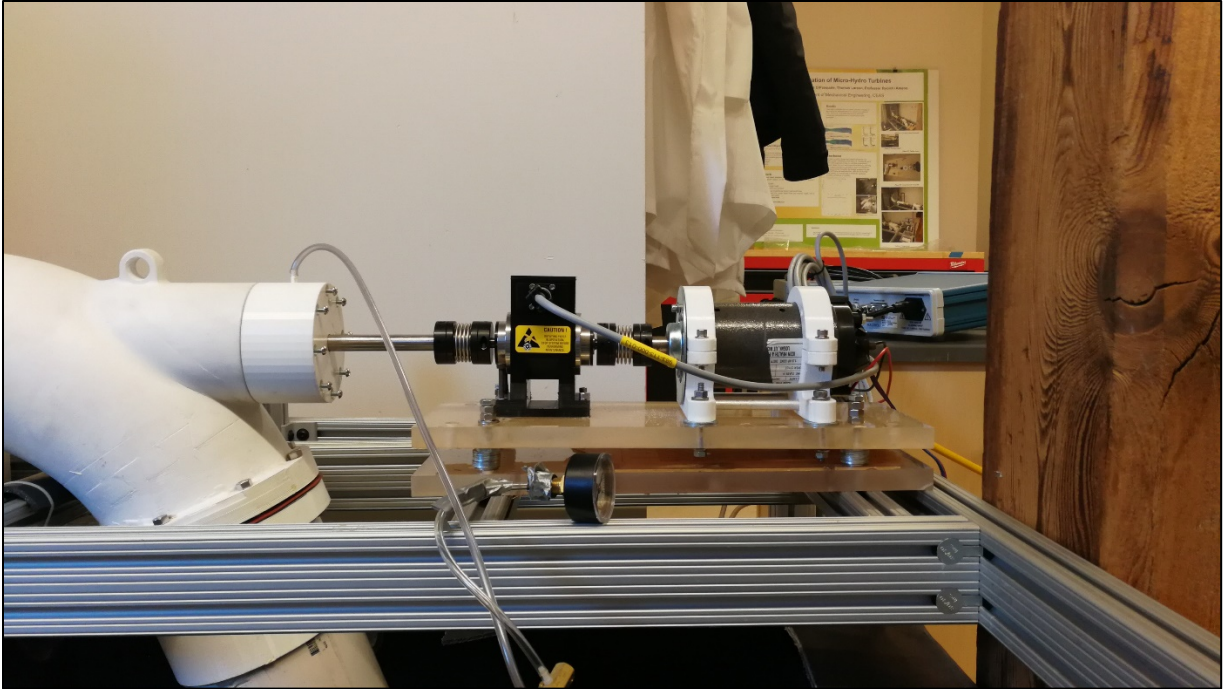
Figure 21: Shaft, torque-meter, and motor assembly

The hydro turbine parts including the stator, rotor, and runner were designed and optimized through previous research conducted at the Hydro Turbine lab. These parts along the exit elbow, air injection chamber and supports were 3-D printed using Eastman Amphora 3-D Polymer AM3300 commercialized by ColorFabb as nGen [42]. Figure 22 exhibits the 3-D printed 3-inch turbine rotor. The parts were designed and optimized using a Computer Aided Design (CAD) modeling software to match with the system configuration and requirements. Ultimaker 2+ [43] was utilized to 3-D printer the turbine parts and supports used in the experimental setup.

Figure 22: 3-D printed 3-inch turbine rotor

3.2 Air Injection Design

The system was designed to introduce air at the suction side of the rotor blades. However, the way the setup was configured provided flexibility to test different turbine designs as well as various air injection techniques.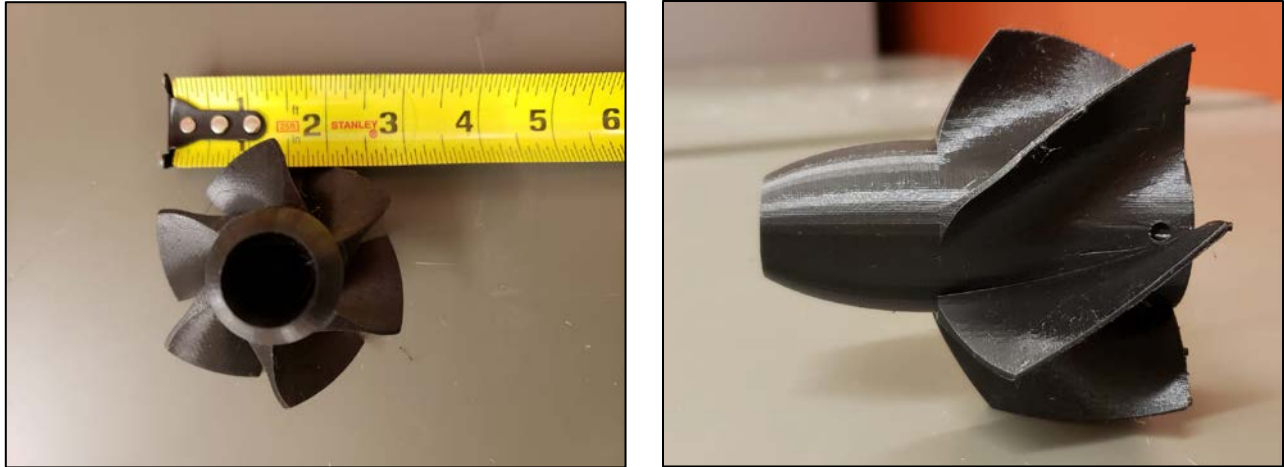 To enable this feature while having rotating parts, the shaft was utilized as a media to transport the air to the turbine rotor. A hollow shaft was selected to have a channel for aeration purposes in addition to measuring the power generated through the turbine. Air is injected into an air-tight chamber attached to the exit elbow as shown in CAD drawing in Figure 23.

Air tightness and sealing the chamber was achieved using two ceramic ball bearings attached to the shaft at both ends of the air injection chamber. Two holes were drilled in the shaft at the air injection chamber providing entry points for the air to the passage intended for the air to be delivered to the rotor. Both ends of the shaft air passage were terminated and blocked permanently preventing the air to escape and forcing it to travel to the turbine rotor.
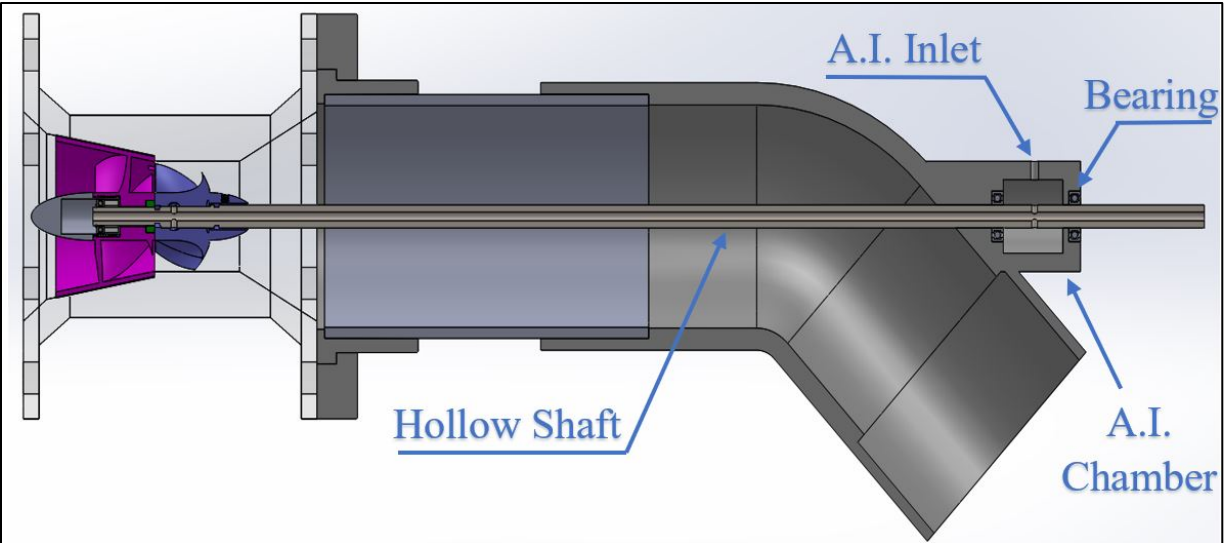
Figure 23: Air injection technique CAD drawing – section view

Additionally, the shaft was machined at the other end to be interlocked with the turbine rotor as well as drilling two holes permitting the air to be injected at the leading edge of the rotor. The design of the rotor incorporated channels to provide a passage for the air to be injected at the suction side of the blades. The channels were designed to distribute the air to the five 3mm-diameter air injection ports as indicated in Figure 24.
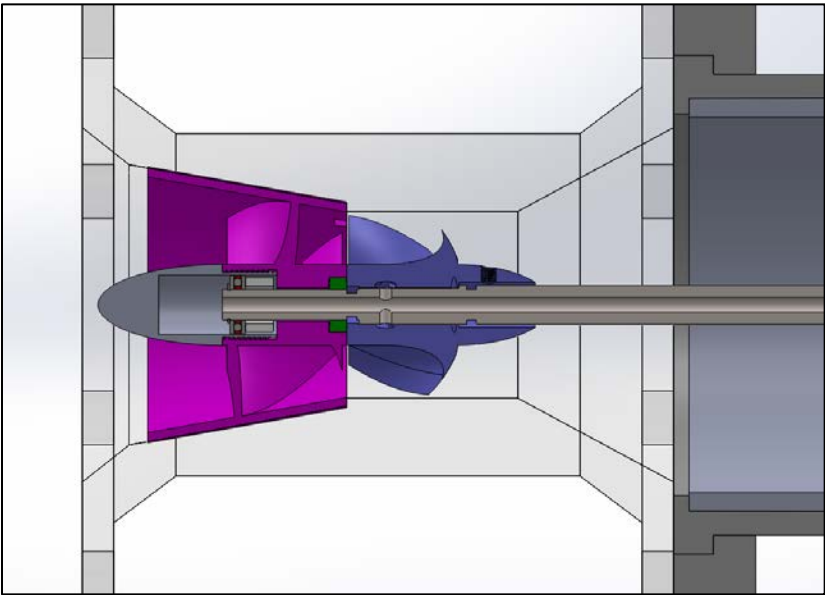
Figure 24: Air injection at turbine rotor CAD drawing – section view

Compressed air was utilized in the air injection process. The lab is served with 551.6 kPa (80 psi) compressed air network that is distributed throughout the whole facility. Hoses were used to transport the compressed air from the air nozzle taps to the air injection chamber as shown in Figure 25. Air pressure was measured using a pressure gauge connected to the air distribution manifold.
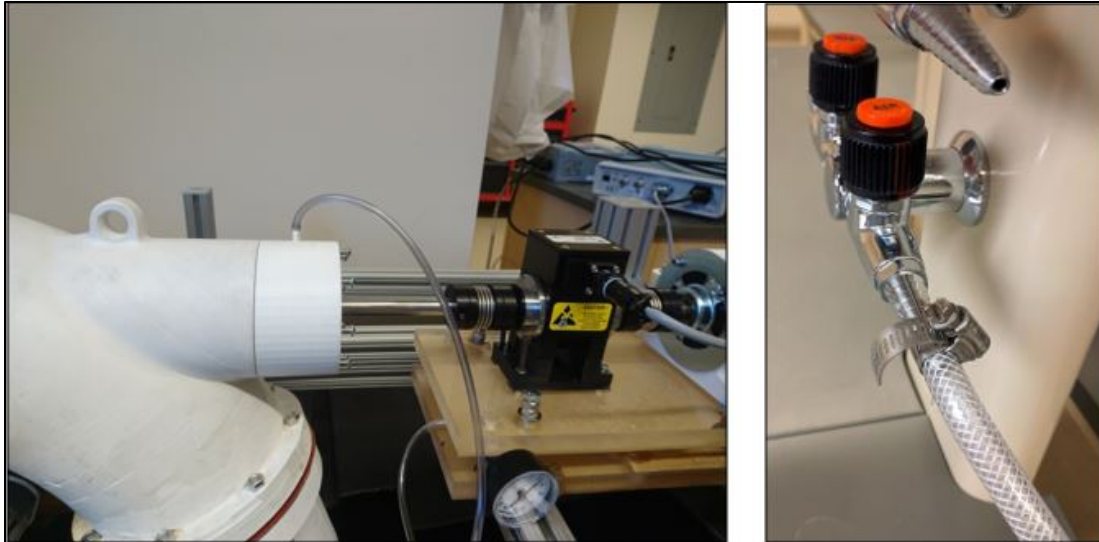
Figure 25: Air injection chamber and compressed air tap

3.3   Instrumentation

3.3.1 Ultimaker 2+

Ultimaker 2+ is a 3-D printer with a printing platform of 223 x 223 x 205 mm that has the capability to print complex 3-D parts at various layer resolutions. The printer has a high flexibility and provides a wide range of filament materials in addition to printing nozzle sizes. The printing layer resolution can be as fine as 0.6mm and the maximum printing speed can reach up to 24 mm^3/s [43]. Figure 26 shows the 3-D printer that were utilized to print the parts used in building the experimental setup.

Figure 26: Ultimaker 2+ 3-D printer

3.3.2 FASTCAM Mini UX50

Flow and cavitation can be captured using a high-speed camera that is capable of taking thousands of images in one second. The high-speed camera is considered a powerful tool, through image processing, in analyzing the different pattern of cavitation and physics, that can be seen in a slow-motion frame. The high-speed camera that was utilized in the experimentation, ISO 10,000 monochrome FASTCAM Mini UX50, is capable of capturing images up to 102,400 fps. The highest image resolution is 1280 x 1024 pixels which can be achieved with a 2000 fps [44]. The camera can be connected to a computer to process and enhance the images captured through a special software developed for the camera. The high-speed camera is shown in Figure 27.

Figure 27: High-speed camera

3.3.3 Flow Meters

Flow rates in the experimental setup were monitored via two electromagnetic flow meters. A 3-inch (0.076m) flow meter were installed on the pump discharge pipe that fills the upper tank and a 2-inch (0.051m) were installed on the overflow line of the upper tank. The difference between the two flow rates gives the flow rate going through the turbine while maintaining a constant head. The M-2000 M-series Mag Meter manufactured by Badger Meter were used in the experimentation. The meter has two DC-powered electromagnetic coils and set of electrodes that create a magnetic field and senses when a conductive fluid like water passes through the meter. The voltage difference between the electrodes is directly proportional to the average velocity of the fluid and then converted to a flow rate. The meter has an accuracy of ±0.25% [45]. Figure 28 exhibits the installed flow meters on the system.
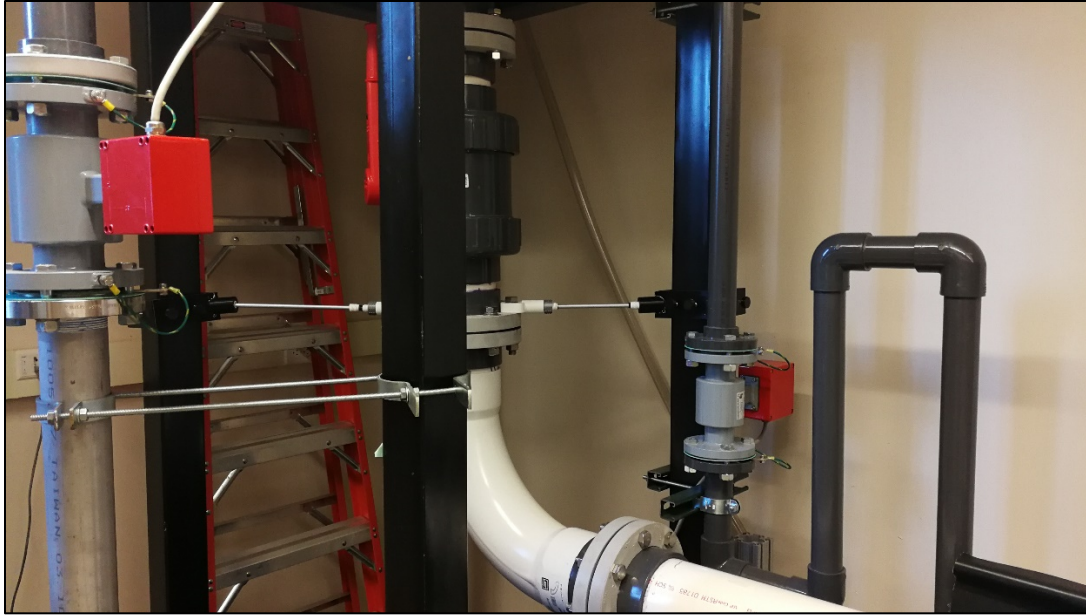
Figure 28: Flow meters installed on the filling and overflow lines

3.3.4 Torque Meter and Torque Display

Torque is measured through an inline torque transducer that is connected to the shaft using a non-slip coupling. The Magtrol TM300 series was utilized to obtain the torque and rotational speed measurements. The non-contact differential transformer has an integrated conditioning electronic module providing a 0 to ±10 VDC torque output as well as a speed output with an accuracy less than 0.1% [46]. The torque meter was connected to a torque display device that provided the torque, power, and rotational speed measurements. The Magtrol 3411 Torque Display was employed and connected to the torque meter to gather the pertinent data. The device uses a high-speed processer to display the measurements as well as powering the transducer with an accuracy of 0.01% for speed and 0.02% for torque readings [47]. The torque transducer and display are shown in Figure 29.
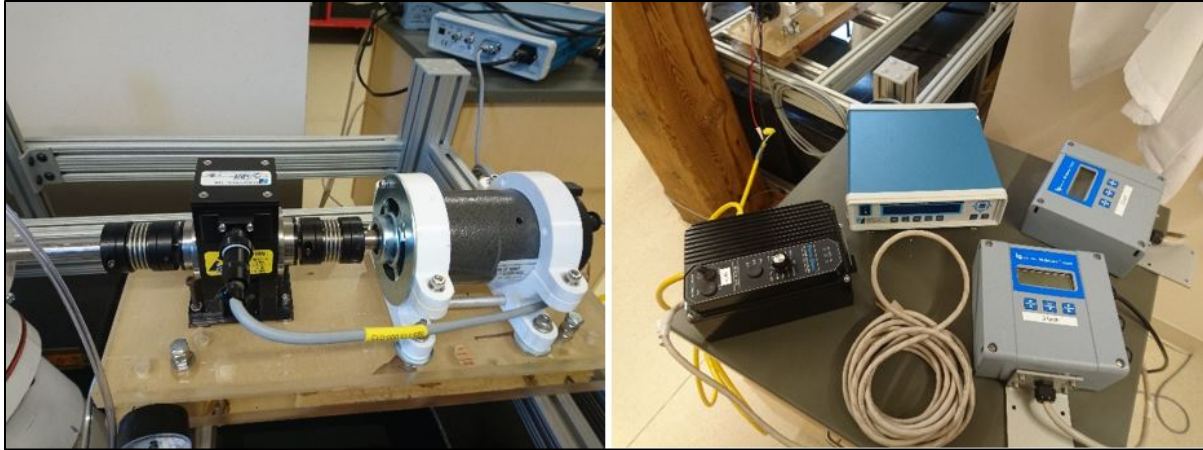
Figure 29: Toque transducer and display device

3.3.5 DC Motor and Motor Controller

The other side of the torque transducer, as shown in Figure 29, was connected to a 2.25 HP (1678 W) DC motor that can be re-wired to be used as a generator. The permanent magnet with brushes motor can reach up to 5135 rpm at 130 VDC at no load [48]. The motor can be equipped with a Variable Speed Drive (VSD) to control the motor speed. The NEMA 4X/IP65 PENTA-DRIVE controller utilized in the setup has the capability to control the speed of DC motors from sub-fractional up to 5 HP [49]. Figure 30 shows the motor and the VSD that were used in the lab.
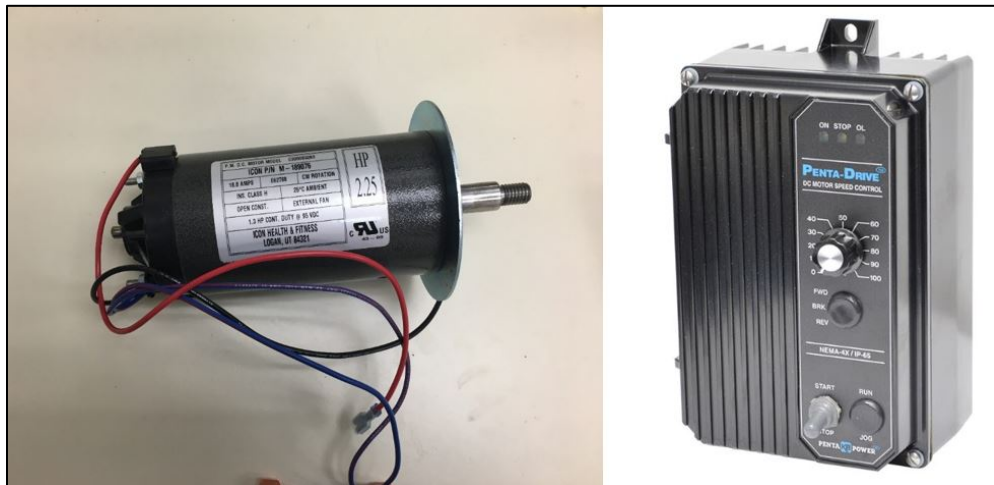
Figure 30: DC motor and VSD

3.3.6 Variable Speed Driven Pump

The water was lifted from the lower (sink) tank to the upper tank via a 10 HP (7460 W) close-coupled centrifugal pump. The 4250 ATM pump can provide flow rate up to 7.93 m³/s (500 GPM) and a maximum head of 30 m (98.4 ft) [50]. The pump is equipped with a VSD to provide a closed control flow rate during the experimental testing. The ABB ACS310-03U-34A1-2 VSD is capable of controlling motors ranging 7.5 – 10 HP with a digital output accuracy of 0.2% [51]. It also has the capability to change the speed manually as well as programmable control to provide an energy-efficient operation. The pump and the VSD installed in experimental setup are indicated in Figure 31.

Figure 31: Pump-motor set and VSD

3.4   Numerical – Experimental Validation

3.4.1 Approach

The results obtained through the CFD simulations were compared with the measurements and data captured during the experimental tests. The verification of the CFD results is necessary to ensure the accuracy and credibility of the simulations conducted prior to the experimentations.

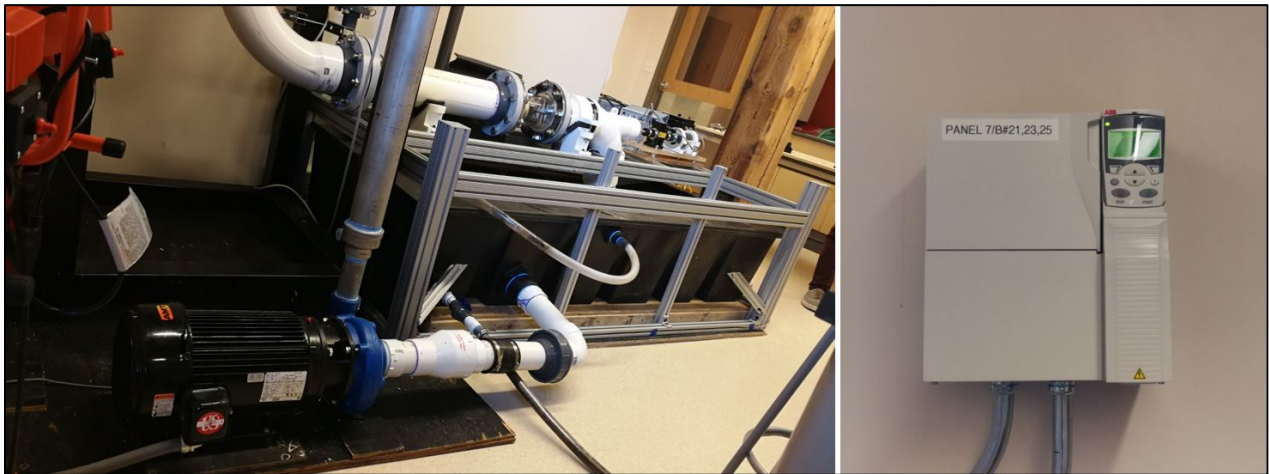However, the experimental setup had some limitations in terms of the flow rates and head, thus cavitation could not be obtained via running the rotor as a turbine case. Therefore, the DC motor was used to induce the cavitation through operating the setup as a propeller to spin the rotor; power consumption mode. The propeller was allowed to rotate in the same direction as a turbine would, however, with the aid of the motor. The speed of the motor was controlled by the VSD achieving 2000 and 3000 rpm rotational speed.

Therefore, new CFD models were executed to simulate the propeller case as conducted in the experimental runs. The results from the CFD simulations were used in the comparison and validation of the air injection treatment method. The approach of the comparison and validation is illustrated in Figure 32.

Figure 32: Results comparison and validation approach

3.4.2 Visual Validation

The first step in the comparison of the CFD and experimental results were done through analyzing the flow and cavitation patterns. The VVF scenes that were obtained through the propeller case CFD simulations were used to find the similarities with the images of the experimental testing obtained via the high-speed camera. The visual resemblance provided a primitive validation of the CFD results.

3.4.3 CFD Simulation Results

The results obtained through the new set of CFD models that were conducted to simulate the propeller case were used as a second step in the comparison and validation. The power consumption was monitored and observed throughout the CFD simulations to be compared with the values obtained experimentally. The simulations incorporated the same conditions that were attained during the experimental run and simulated the same parameters to ensure the accuracy and reliability of comparison and validation process. Additionally, the VVF scenes obtained were used in the validation process as explained in the following section 3.4.4 Image Processing.

3.4.4 Image Processing

The images obtained from the high-speed camera were processed to quantify the percentage of the cavitation that occurred during the experimental testing. The grayscale images were converted to binary images making it more visible for estimating the cavitation around the turbine blades. This process was done using a computer code that enhances the images and quantify the different color percentages via signal processing.

Image processing started with breaking the image into small sections and improve their contrast. Then, the color intensity was mapped by setting an upper- and lower-pixel values of the grayscale images making the dark spots looks darker and the light spots lighter to enhance the contrast. After that, the images were converted from grayscale to binary images using (1) as logical true and (0) as logical false for each pixel, where (1) represents cavitation. The threshold value between the two values was obtained through iteration and after comparing the cavitation cloud size of different threshold values.

The area was then determined by the size of the image in pixels. The cavitation area was estimated by summing all the true logic (1) values in the image. Then the percentage of the cavitation area was obtained by dividing the cavitation area by the total area in pixels. This process was repeated for 10 images as to visualize the cavitation propagation at different sections of the turbine. Each 10 consecutive images represented one full rotation of the turbine. Finally, a color range was applied to represent the grayscale values in 256 colored images for improved visualization and providing another enhanced validation technique.

4. Results and Discussion

4.1　CFD Results: Constant Water Inlet Velocity

4.1.1　General

The initial CFD simulations, constant water pressure inlet, were not used in the results analysis. As mentioned in Chapter 2, they were used to obtain the water inlet velocities per each rotational speed. The velocities, indicated in Table 4, were utilized in the second CFD simulations as a boundary condition. The result of the cases discussed hereafter are all related to the constant water inlet velocity boundary condition simulations. VVF values were used to investigate the cavitation and were categorized based on the area: blades and hub. Blades VVF corresponds to the vapor volume fraction that formed on the rotor blades, while the hub VVF corresponds to the vapor volume fraction that formed on the rotor hub. Also, the CFD scenes and results resemble the averaged values of the last two cycles in each simulation.

4.1.2　Case 1: No Aeration

The first run of the CFD simulations were conducted without aeration to obtain the data pertaining the cavitation and power generation. This case is considered as the "baseline" in which the data gathered were compared to the values generated by air injection models. Figure 33 represents a single-blade VVF scenes for all rotational speeds (1000 to 5000 rpm). The VVF is represented on a scale of $0 - 1$, where 1 indicates 100% water vapor area and denoted in red color as can be seen in Figure 33 (f). The area representing the blades VVF increases with increasing the rotational speed as it can be inferred from the VVF scenes. As the rotational speed increases,

the pressure drops below the vapor pressure leading to more cavitation. Moreover, the cavitation cloud is being "pushed away" towards the upper edge of the blade as the rotational speed increases. This phenomenon occurred due to the increase in the centrifugal forces that led to pushing out the cavitation cloud as well as having higher velocity at the blade tip.

Figure 33: Blades VVF CFD scenes – no aeration case: (a) 1000 rpm, (b) 2000 rpm, (c) 3000 rpm, (d) 4000 rpm, (e) 5000 rpm, (f) Mean of volume fraction of water vapor scale

However, the hub VVF showed a different trend. The hub VVF decreased with increasing the rotational speed as a result of the centrifugal forces. Additionally, the reduction in the hub VVF can be explained by the pressure scenes in Figure 34. The absolute pressure around the hub tends to increase as the rotational speed increases. The dark blue areas represent the areas where the absolute pressure is equal or less than the water vapor pressure (3170 Pa) as shown in Figure 34(f).
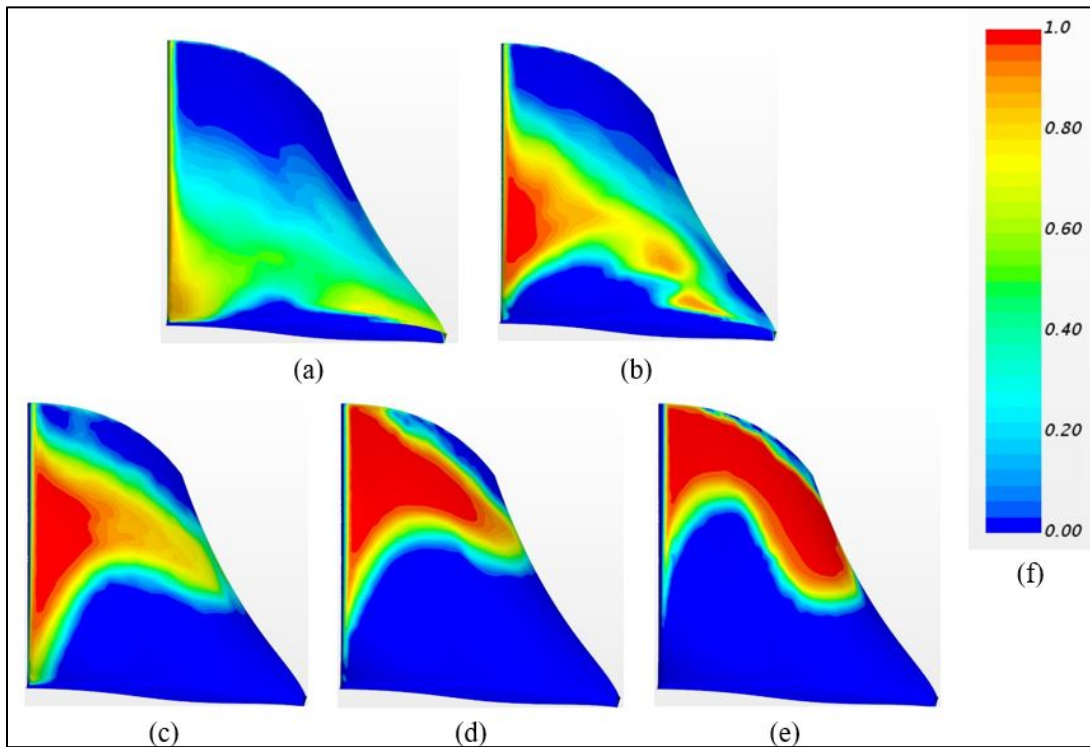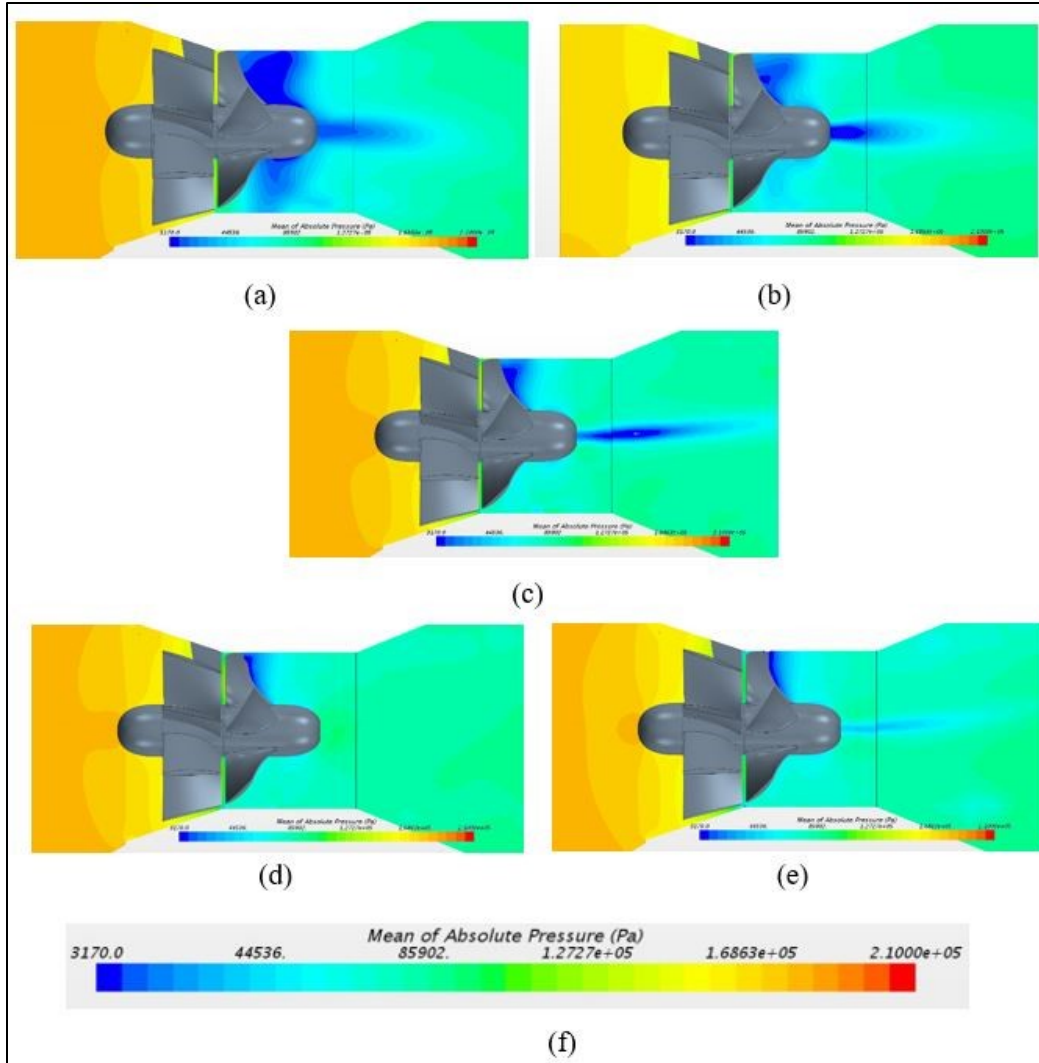
Figure 34: Absolute pressure CFD scenes – no aeration case: (a) 1000 rpm, (b) 2000 rpm, (c) 3000 rpm, (d) 4000 rpm, (e) 5000 rpm, (f) Mean of absolute pressure (Pa) scale

The results of the no aeration case are summarized in Table 5. As indicated previously, the blades VVF increased with the increasing the rpm while the hub VVF decreased. The power generated through the turbine increased as the rotational speed increased reaching the climax at 4000 rpm with a value of 1844.4 W then declined to 1728. W at 5000 rpm.

Table 5: No aeration case summary of CFD results

RPM	Water Inlet Velocity (m/s)	Blades VVF	Hub VVF	Power (W)
1000	2.00	0.0878	0.0851	611.2
2000	2.15	0.1039	0.0049	1128.7
3000	2.29	0.1171	5.018E-06	1607.6
4000	2.45	0.1245	2.746E-09	1844.4
5000	2.64	0.1460	8.743E-10	1728.3

4.1.3 Case 2: 0 PSI Air Injection

The first aeration case was conducted with air injection at 0 psig (101.3 kPa) as to investigate the effect of adding a minimal amount of air. Same cavitation behavior was observed as in the no aeration case. However, it can be inferred from Figure 35 that the areas representing the cavitation were reduced in each rotational speed when compared with the no aeration case. The reduction in the blades VVF was more noticeable at higher rotational speeds (4000 and 5000 rpm). It can be justified by the fact that the blades VVF at the 4000 and 5000 rpm have higher values than the remaining rotational speeds. Yet, the blades VVF in the 1000, 2000 and 3000 rpms were also reduced.
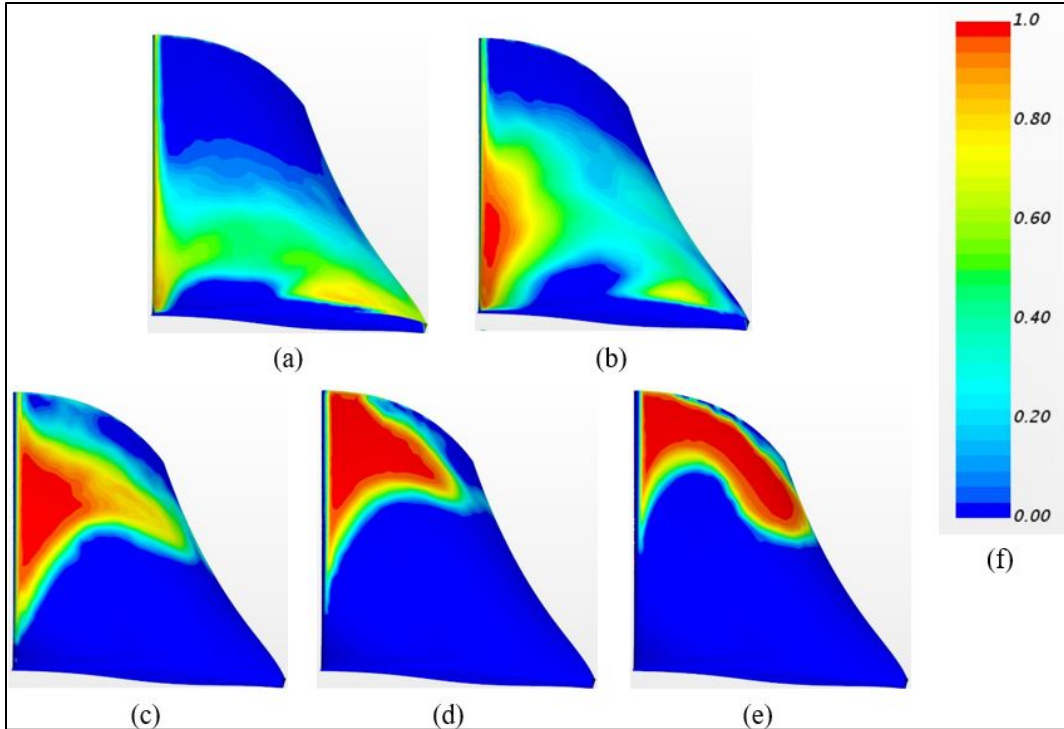
Figure 35: Blades VVF CFD scenes – 0 PSI A.I. case: (a) 1000 rpm, (b) 2000 rpm, (c) 3000 rpm, (d) 4000 rpm, (e) 5000 rpm, (f) Mean of volume fraction of water vapor scale

As for the hub VVF, higher reduction percentage was observed than in the blades VVF. The absolute pressure scenes in Figure 36 indicated that the areas in which the absolute pressure is less or equal to the vapor pressure were reduced when compared to the no aeration case. Moreover, the reduction of the hub VVF while increasing the rotational speed was also noticeable and in concurrence to the no aeration case. Thus, it can be deduced that even a minimal air injection can lead to a quantifiable reduction in the cavitation.

Figure 36: Absolute pressure CFD scenes – 0 PSI A.I. case: (a) 1000 rpm, (b) 2000 rpm, (c) 3000 rpm, (d) 4000 rpm, (e) 5000 rpm, (f) Mean of absolute pressure (Pa) scale

Table 6 lists the results of the blades VVF, hub VVF, and the power generation of the 0 psig air injection case. The blades VVF showed an average reduction of 25.3% when compared to the no aeration case, whereas, the hub VVF showed a reduction of 65.1%. The power was also reduced when compared to the no aeration case with an average reduction of 11.4%. The reduction in the power is due to introducing another substance, i.e. air, that caused reaction forces opposing

the rotation of the turbine. Thus, to maintain the same rotational speed, the power generated was reduced.

Table 6: 0 PSI A.I. case summary of CFD results

RPM	Water Inlet Velocity (m/s)	Blades VVF	Hub VVF	Power (W)
1000	2.00	0.0767	0.0646	580.8
2000	2.15	0.0796	2.17E-05	1045.1
3000	2.29	0.0857	6.431E-09	1470.1
4000	2.45	0.0949	7.323E-10	1589.5
5000	2.64	0.0960	6.251E-10	1446.1

4.1.4 Case 3: 3 PSI Air Injection

Air pressure was increased in the second case of aeration to 122.0 kPa (3 psig). The cavitation pattern did not change from the two previously discussed cases and showed even better results. The cavitation cloud is being pushed even farther towards the blades tip with increasing the rotational speed. Additionally, the cavitation was increased while the rotational speed goes up. Figure 37 indicates a reduction of the blades VVF when compared to the no aeration case. It can be observed that the blades VVF is less than the no aeration which is also in agreement with the 0 psig air injection case.
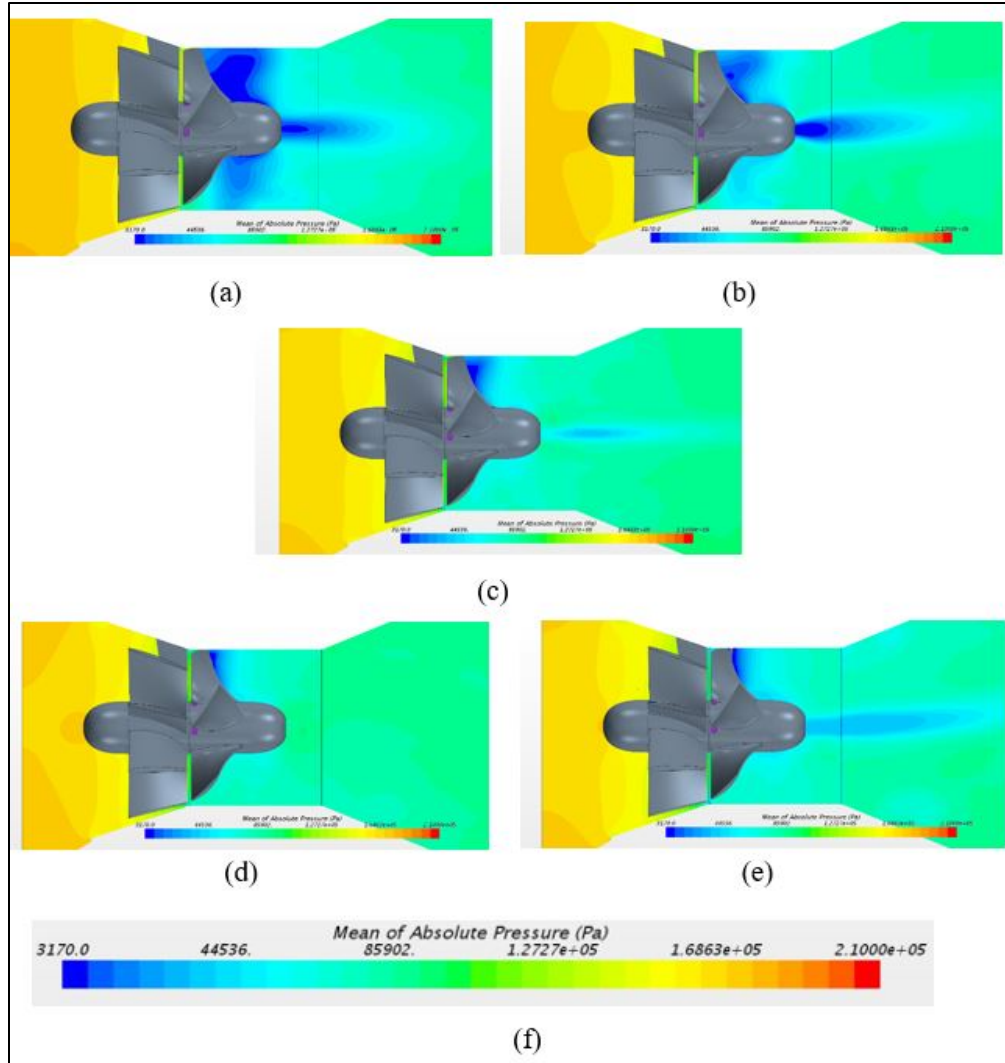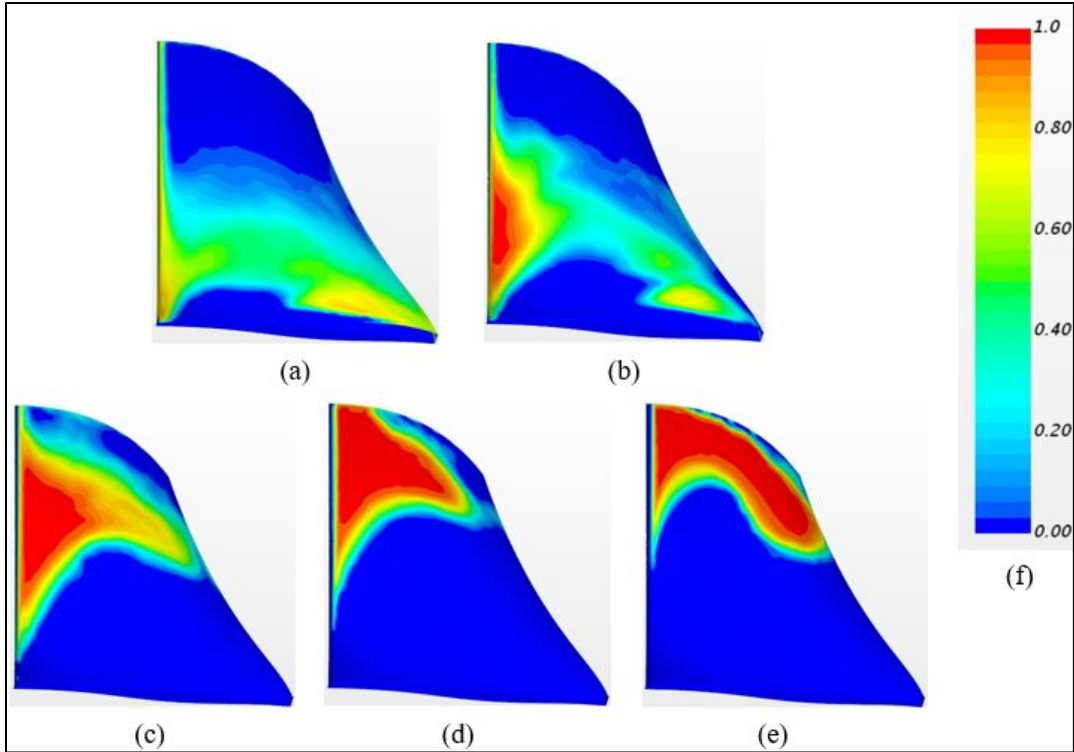
Figure 37: Blades VVF CFD scenes – 3 PSI A.I. case: (a) 1000 rpm, (b) 2000 rpm, (c) 3000 rpm, (d) 4000 rpm, (e) 5000 rpm, (f) Mean of volume fraction of water vapor scale

The pressure scenes in Figure 38 shows a reduction in the hub VVF with increasing the rotational speed. The blue color that refers to the areas in which the absolute pressure is equal or less than the water vapor pressure (3170 Pa) was reduced by the air injection. This is confirmed when looking at the no aeration case and is more obvious when comparing the pressure at the 1000, 2000, and 3000 rpm scenes.
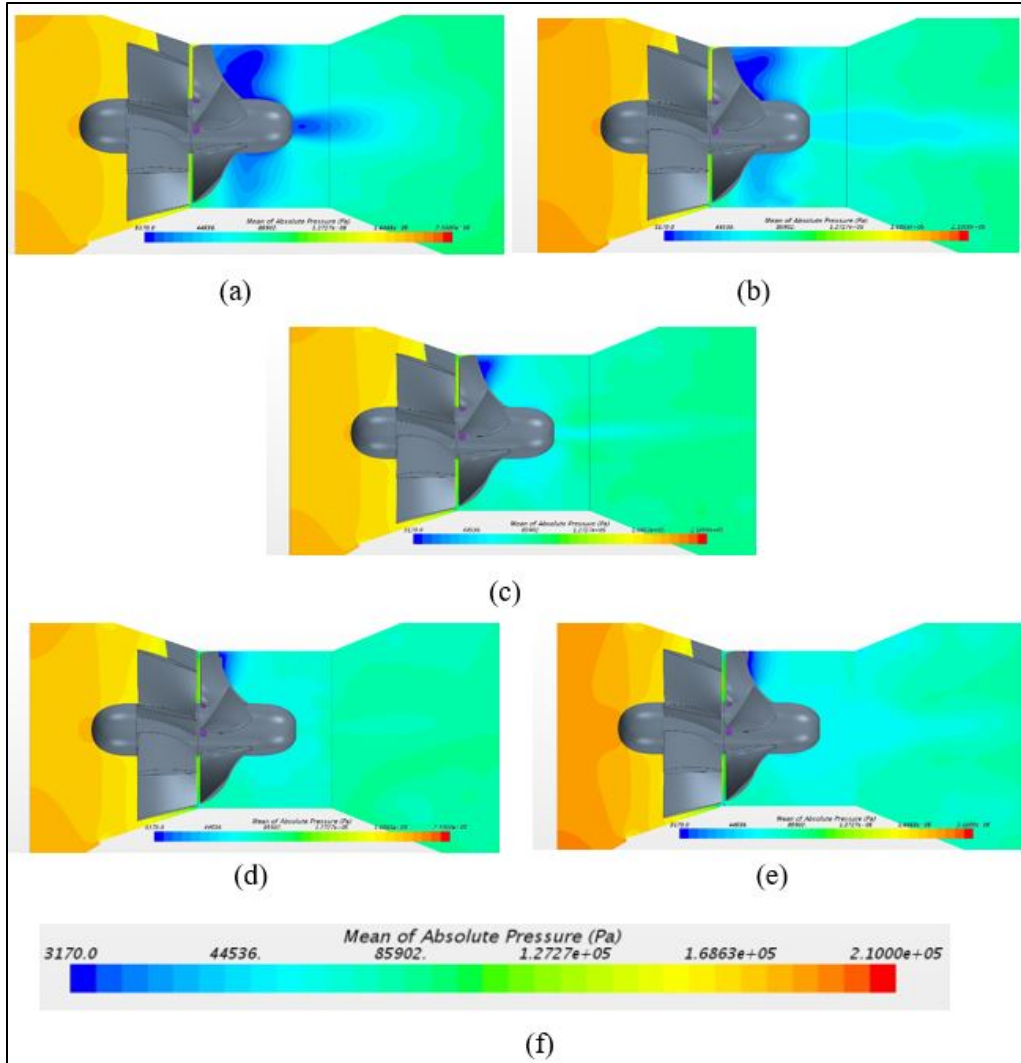
Figure 38: Absolute pressure CFD scenes – 3 PSI A.I. case: (a) 1000 rpm, (b) 2000 rpm, (c) 3000 rpm, (d) 4000 rpm, (e) 5000 rpm, (f) Mean of absolute pressure (Pa) scale

The average reduction in the blades VVF is 33.6% with comparison to the no aeration case, while the hub VVF was reduced by 73.1%. The power was also reduced when compared to the no aeration case with an average reduction of 8.9%. Although the blades and the hub VVFs, resembling the cavitation, were decreased leading to an improved case, however, the power was also reduced. The highest power generated while injecting the air at 3 psig 1605.4 W at 4000 rpm

53

was reduced compared to the no aeration case with 1844.4 W. The average reduction in the power

compared to the no aeration case is 9.5%. The results of the blades VVF, hub VVF, and the power

generation of the 3 psig air injection case are summarized in Table 7.

Table 7: 3 PSI A.I. case summary of CFD results

RPM	Water Inlet Velocity (m/s)	Blades VVF	Hub VVF	Power (W)
1000	2.00	0.0727	0.0492	591.2
2000	2.15	0.0749	3.51E-06	1051.7
3000	2.29	0.0757	2.092E-09	1473.5
4000	2.45	0.0780	6.150E-10	1605.4
5000	2.64	0.0835	4.749E-10	1540.0

4.1.5 Case 4: 5 PSI Air Injection

The last CFD simulations case that was conducted investigated air injection at 135.8 kPa

(5 psig). The blades VVF scenes of the five rotational speeds for the 5 pisg air injection case are

shown in Figure 39. As observed, the blades VVF scenes followed the same pattern of the 0 psig

and 3 psig air injection cases. The cavitating area is being pushed farther reaching to the blades tip

as the rotational speed increases. Also, the area representing 100% water vapor - red colored areas,

was decreased in regard to the no aeration case. The cavitation reduction is noticeable at every

rotational speed and increasing the air pressure is causing the cavitation to diminish by increasing

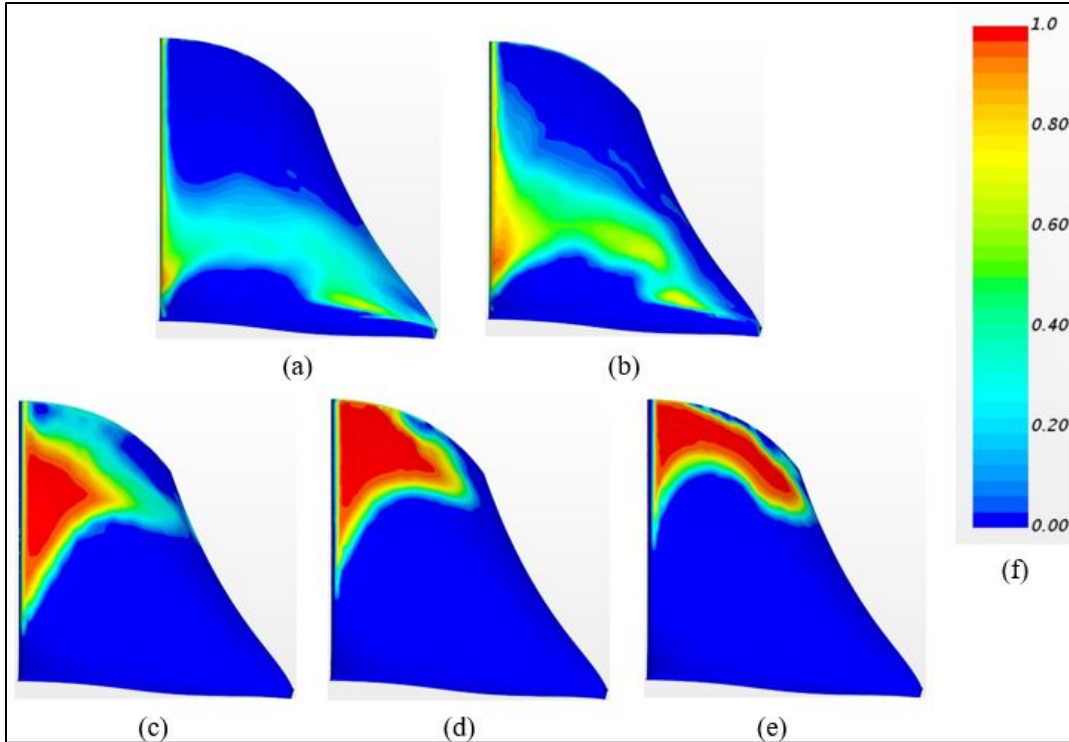the pressure at the suction side of the rotor blades.

Figure 39: Blades VVF CFD scenes – 5 PSI A.I. case: (a) 1000 rpm, (b) 2000 rpm, (c) 3000 rpm, (d) 4000 rpm, (e) 5000 rpm, (f) Mean of volume fraction of water vapor scale

The hub VVF behavior was not deviated from the previously discussed cases. The pattern can be explained using the pressure scenes at each rotational speed as indicated in Figure 40. At lower speed, 1000 and 2000 rpms, the hub is surrounded by a blue colored area which refers to areas where the absolute pressure is around the water vapor pressure. As the speed increases, the blue colored area around the hub disappears and just observed around the tip of the rotor blades which is in concurrence with the blades VVF scenes shown in Figure 39. Furthermore, the pressure in the 5 psig air injection case is higher than the no aeration case at every rotational speed. The increase in the pressure led to reducing the hub VVF and thus less cavitation occurred.
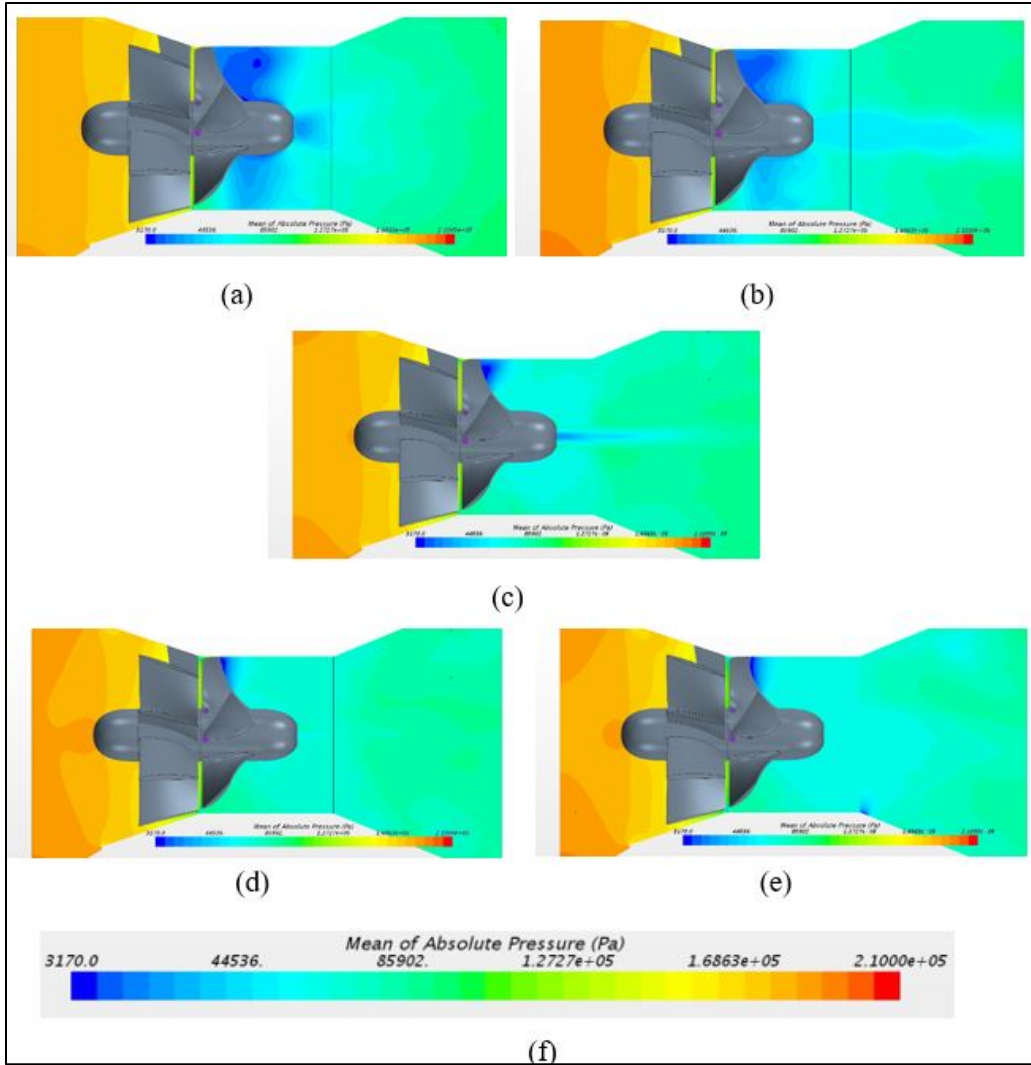
Figure 40: Absolute pressure CFD scenes – 5 PSI A.I. case: (a) 1000 rpm, (b) 2000 rpm, (c) 3000 rpm, (d) 4000 rpm, (e) 5000 rpm, (f) Mean of absolute pressure (Pa) scale

The CFD simulation results of the 5 psig air injection are outlined in Table 8. Compared to the no aeration case, the 5 psig air injection case achieved an average blade VVF reduction of 49.7%, whereas the hub VVF was reduced by 90.6%. For instance, the no aeration blades VVF at 5000 rpm was 0.1460, while the 5 psi air injection blades VVF was 0.0686 at 5000 rpm. The maximum power generated was 1681.6 W at 4000 rpm, whereas 1844.4 W for the no aeration case. The 5 psig air injection case led to an average power generated of 6.6% from the no aeration.

56

Table 8: 5 PSI A.I. case summary of CFD results

RPM	Water Inlet Velocity (m/s)	Blades VVF	Hub VVF	Power (W)
1000	2.00	0.0465	0.0282	601.9
2000	2.15	0.0475	4.420E-08	1066.0
3000	2.29	0.0633	9.588E-10	1504.1
4000	2.45	0.0654	9.694E-11	1681.6
5000	2.64	0.0686	8.939E-11	1610.1

4.1.6 Results Comparison

To have a better understanding of the correlation between the cavitation and injecting air at different pressures, the blades VVF scenes at the same rotational speed were examined more thoroughly. Figures (41 – 45) show the blades VVF scenes of the four cases at 1000, 2000, 3000, 4000, and 5000 rpm respectively. The Figures indicate that as the rotational speed increased the area which has high VVF values expanded leading to more cavitation. Furthermore, the centrifugal forces, that are induced by the rotating motion of the turbine, caused the cavitation to occur at the tip of the blades, in other words; shifting of the cavitation. This is more distinguished when looking at the 4000 and 5000 rpm scenes.

Moreover, it can be inferred from each Figure that the area of high VVF values were reduced while increasing the air injection pressure. The highest reduction achieved is noticeable at each rotational speed of the 5 psig A.I. case. Thus, it can be concluded that increasing the air injection pressure leads to more treatment of cavitation and improved performance of the turbine on the long run. However, it should be noted that air was introduced by the means of compressed air system which is a major energy consumer. Hence, it will be an expensive approach to treat the cavitation in hydro turbines. Also, increasing the air pressure might lead to air entrainment which also impact the component of the hydro turbine system. Therefore, it is worth to investigate the impact and the feasibility of increasing the air injection pressure.
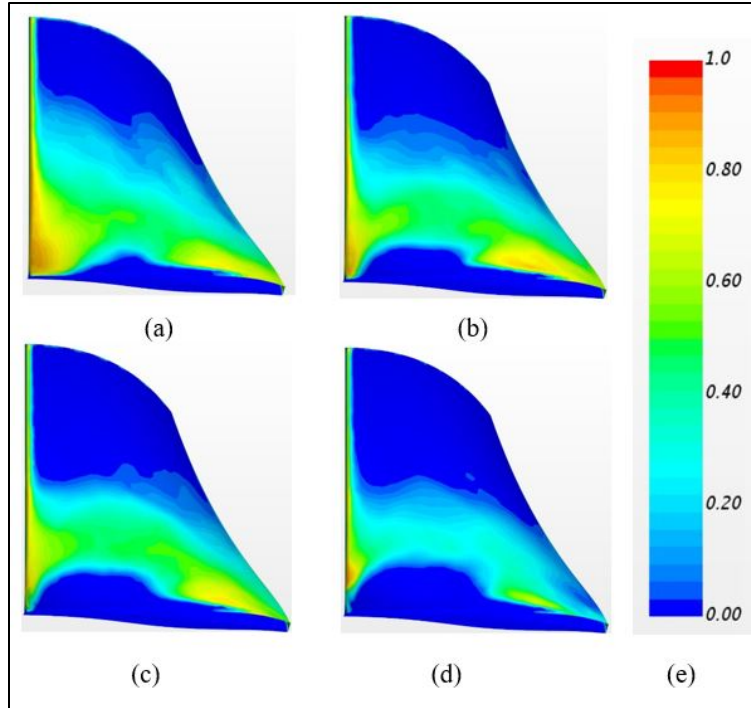
Figure 41: Blades VVF CFD scenes at 1000 rpm: (a) no aeration, (b) 0 psig A.I., (c) 3 psig A.I.,

(d) 5 psig A.I., (e) Mean of volume fraction of water vapor scale

Figure 42: Blades VVF CFD scenes at 2000 rpm: (a) no aeration, (b) 0 psig A.I., (c) 3 psig A.I.,

(d) 5 psig A.I., (e) Mean of volume fraction of water vapor scale

Figure 43: Blades VVF CFD scenes at 3000 rpm: (a) no aeration, (b) 0 psig A.I., (c) 3 psig A.I.,

(d) 5 psig A.I., (e) Mean of volume fraction of water vapor scale

Figure 44: Blades VVF CFD scenes at 4000 rpm: (a) no aeration, (b) 0 psig A.I., (c) 3 psig A.I.,

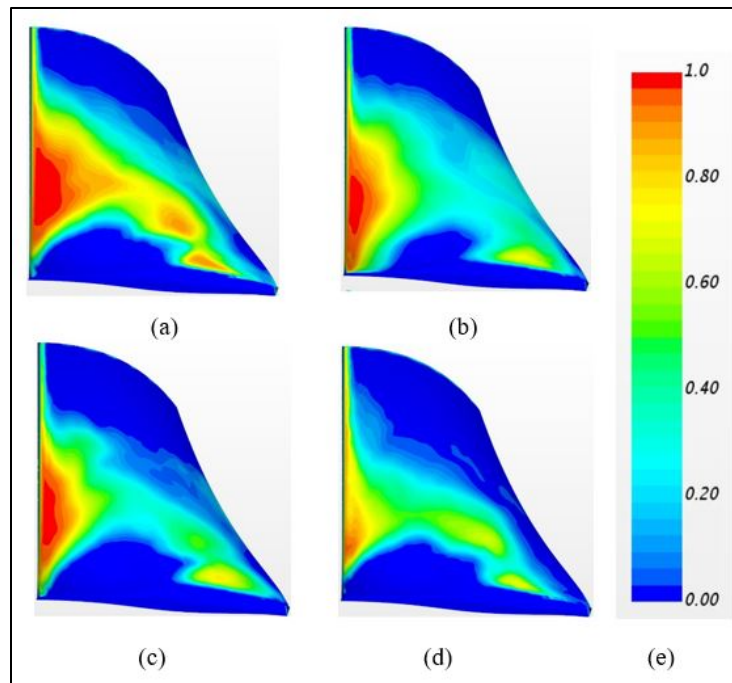(d) 5 psig A.I., (e) Mean of volume fraction of water vapor scale
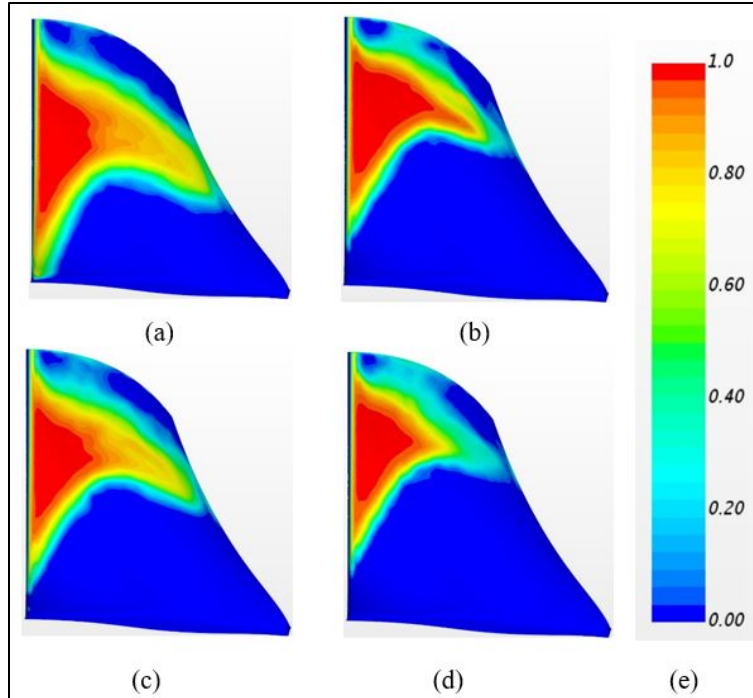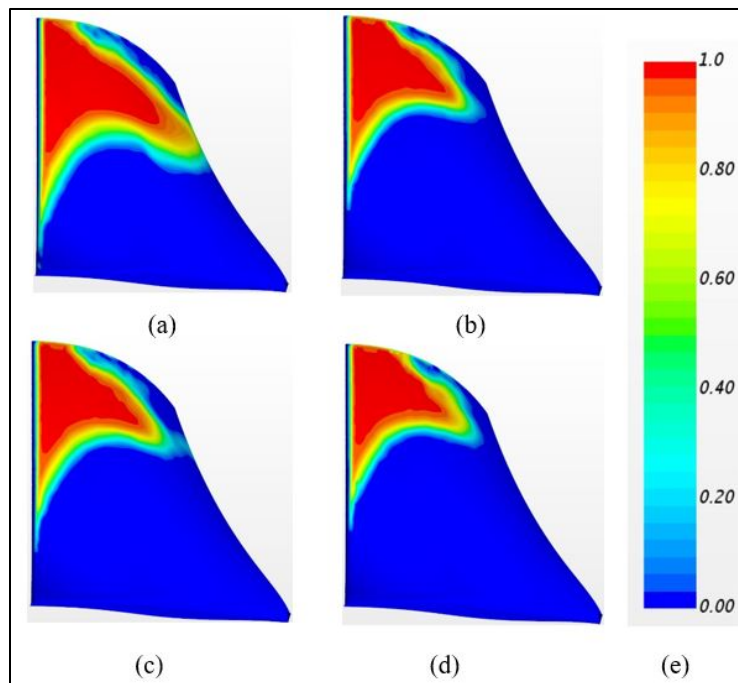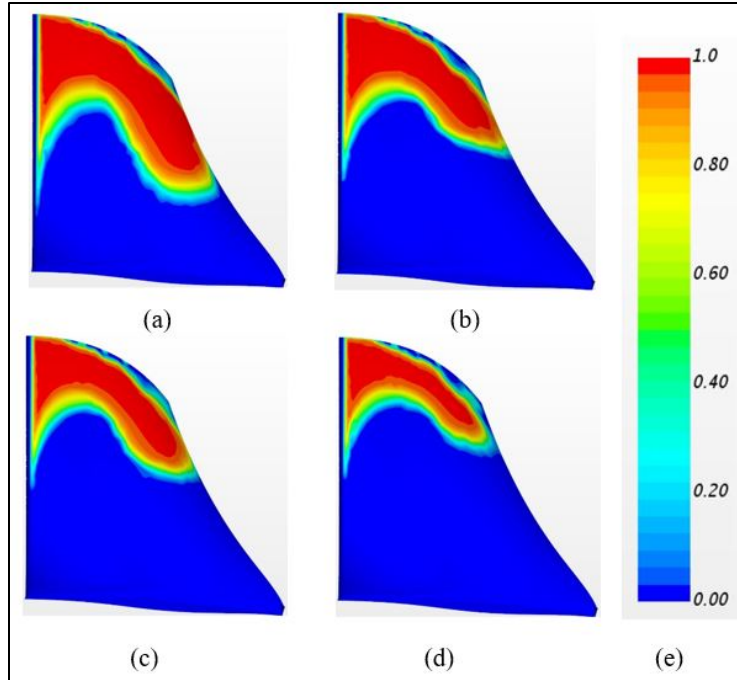
Figure 45: Blades VVF CFD scenes at 5000 rpm: (a) no aeration, (b) 0 psig A.I., (c) 3 psig A.I.,

(d) 5 psig A.I., (e) Mean of volume fraction of water vapor scale

The air injection effect is even more obvious when looking at the Blades VVF against the

rotational speed presented in Figure 46. The blue line representing the no aeration case, which is

the baseline case, had the highest blades VVF reaching up to 0.1460 at 5000 rpm. As air is being

introduced starting from 0 psig up to 5 psig, it can be shown clearly how the air is effectively

treating the cavitation phenomenon while increasing the air pressure in the system. Even with the

smallest amount of air being injected at the leading edge, as in the 0 psig A.I. case, can help in

reducing the cavitation with a considerable amount reaching up to 34.2% at 5000 rpm. The

behavior of the cavitation treatment in the 0 psig and 3 psig cases at the 1000 and 2000 rpm is

almost similar whereas in the 5 psig case the reduction was larger, as shown in the graph. This is

due to the remarkable increase of the absolute pressure in the system at the 5 psig case as seen in

the pressure scenes, leading to a better treatment of cavitation. As the rotational speed increased,

the difference between the three A.I. cases became less than the first two rotational speeds since

60

the cavitation increases at higher speeds. The reduction of the blades VVF at the 5000 rpm was

42.8% in the 3 psig case while maximizing at 53.0% in the 5 psig case.
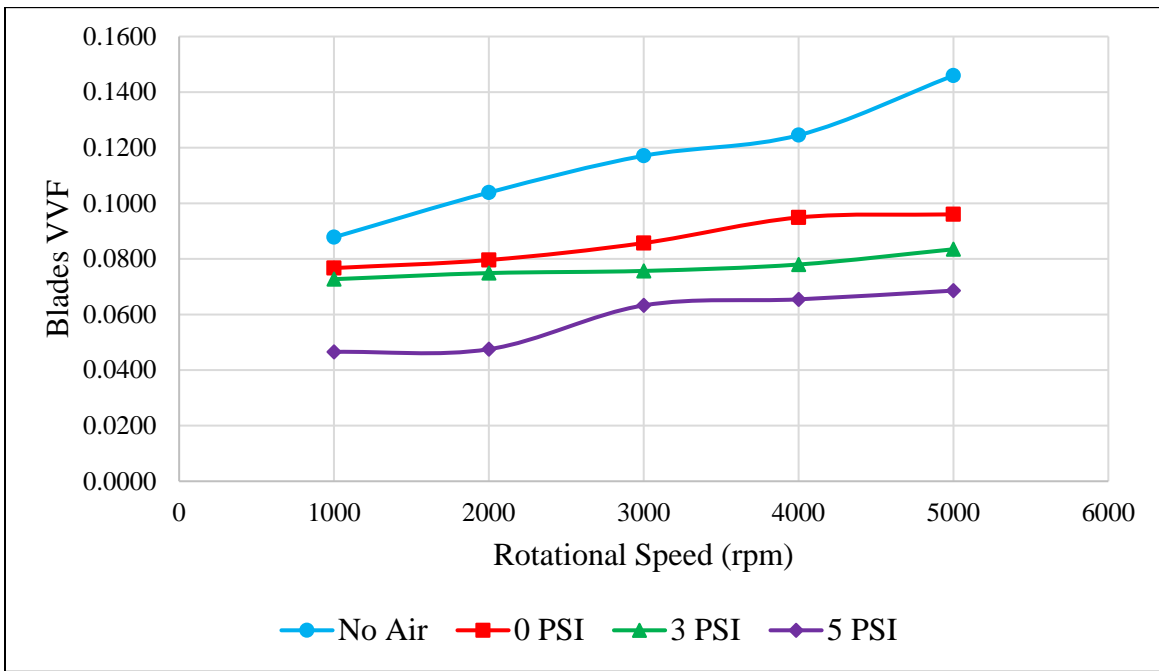

Figure 46: Blades VVF versus rotational speed graph

The VVF comparison was more focused on the blades side than on the hub since the

cavitation behavior tends to decrease drastically on the hub while increasing the rotational speed.

The increase in the centrifugal forces as the rotational speed increased led to increase the pressure

around the hub and thus reducing the cavitation. It was observed in all cases with and without

aeration, as indicated in Table 9, that the hub VVF decreased considerably with increasing the

rotational speed. For instance, the hub VVF at 1000 rpm was 0.0851 whereas 8.743×10^{-8} at 5000

rpm in the no aeration case which is almost 99.99999% reduction. Even with this huge reduction,

air injection successfully reduced the hub cavitation when considering each rotational speed by

itself. For example, at 5000 rpm the hub VVF was reduced by 28.5%, 45.7%, and 89.8% in the 0

psig, 3 psig, and 5 psig A.I. cases respectively.

Table 9: Blades and hub VVF per each rotational speed

RPM	VVF Blades (VVF Hub)			
	No Air	0 PSI	3 PSI	5 PSI
1000	0.0878 (0.0851)	0.0767 (0.0646)	0.0727 (0.0492)	0.0465 (0.0282)
2000	0.1039 (0.0049)	0.0796 (2.173E-05)	0.0749 (3.507E-06)	0.0475 (4.420E-08)
3000	0.1171 (5.018E-06)	0.0857 (6.431E-09)	0.0757 (2.092E-09)	0.0633 (9.588E-10)
4000	0.1245 (2.746E-09)	0.0949 (7.323E-10)	0.0780 (6.150E-10)	0.0654 (9.694E-11)
5000	0.1460 (8.743E-10)	0.0960 (6.251E-10)	0.0835 (4.749E-10)	0.0686 (8.939E-11)

On the other side, the power generation was affected adversely with the air injection. The power was reduced due to introducing air which replaced the water flowing at 2.00 – 2.6 m/s that is responsible to rotate the turbine. Additionally, air injection induced more reaction forces on the turbine which reduced the output power as to maintain the same rotational speed that was set during the simulations. This impact was noticed to be highest at 0 psig A.I. case than the rest of the A.I. cases as indicated in Table 10. The effect of the cavitation treatment influenced the power output since cavitation reduces the power generation, thus, the 0 psig A.I. case showed the least power generation among the A.I. cases. As the air pressure increases, reducing the cavitation, more power is being generated from the turbine while maintaining the no aeration case with the highest power generation, as inferred from Figure 47. Also, with increasing the air pressure the turbine retained part of the power, that was lost via air injection, since the pressurized air increased the absolute pressure in the system as observed from the pressure scenes.

Table 10: Generated power per each rotational speed

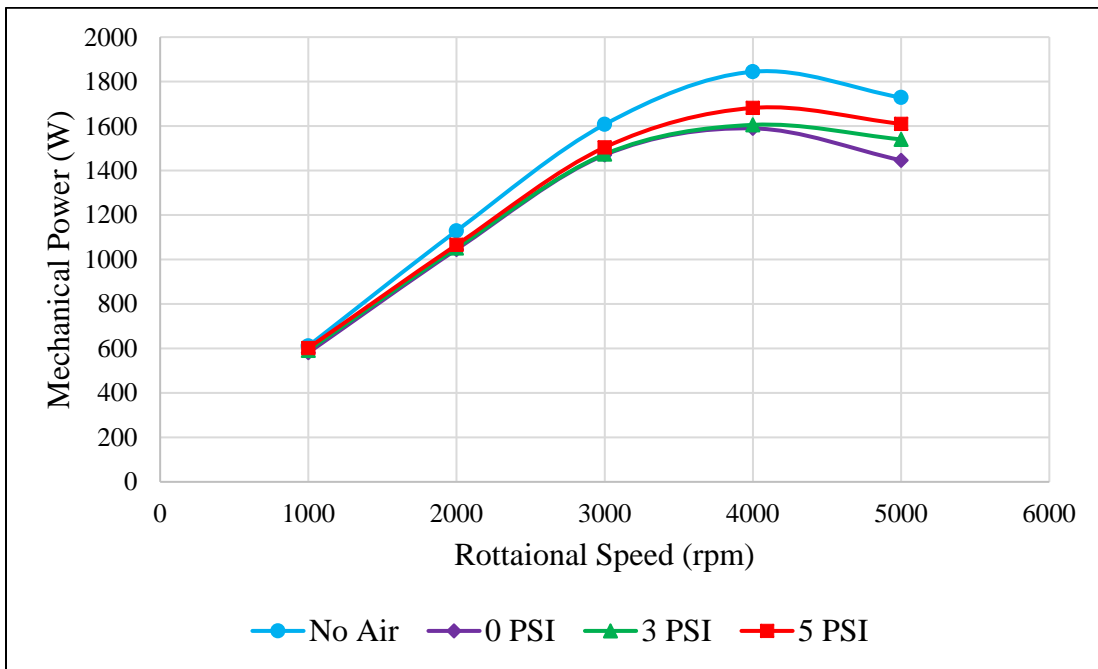| RPM	Generated Mechanical Power (W)			
	No Air	0 PSI	3 PSI	5 PSI
1000	611.2	580.8	591.2	601.9
2000	1128.7	1045.1	1051.7	1066.0
3000	1607.6	1470.1	1473.5	1504.1
4000	1844.4	1589.5	1605.4	1681.6
5000	1728.3	1446.1	1540.0	1610.1

Figure 47: Mechanical power versus rotational speed graph

4.2   Experimental Results

4.2.1 General

As discussed in Chapter 3, due to the experimental setup limitation in inducing cavitation the turbine was forced to rotate in the same direction using a motor thus acting as a propeller. The propeller was forced to rotate at 2000 and 3000 rpm with and without aeration. The air, introduced by a compressed air system that served the lab, was injected at pressures of 0, 3, 5, and 12 psig to investigate the air injection effect. The water flow rate and head were maintained per each rotational speed case as to eliminate any interaction effect that might impact the cavitation behavior.

The propeller was speed were controlled using the motor controller and the system was allowed to stabilize before collecting the data. Once the head was steady and the readings of the different meters were not fluctuating the readings were recorded. The no aeration case data were collected first, and then similar procedures were adopted for the air injection cases. The air injection was monitored through a pressure gauge installed on the compressed air manifold that was also used for air injection. The data collected are water flow rate, head, power, air pressure, and the rotational speed. Additionally, the cavitation pattern was observed through video recording the propeller in the clear housing using the high-speed camera.

4.2.2 Propeller Case – 2000 rpm

The first case of the experimental results is exhibited in Table 11. The power is shown in negative value since it represents the power that was consumed to rotate the propeller. In this case, the power consumed was increased as the pressure of the air injection was increased. The no aeration case had the lowest power consumption and with the addition of the air into the system, the power consumption increased to maintain spinning the propeller at the same rotational speed.

64

Table 11: Propeller 2000 rpm case summary of experimental results

Air pressure (psig)	Water Flow Rate (m³/s)	Head (m)	Power (W)
No air	0.010	2.00	-55.0
0	0.0099	2.00	-56.5
3	0.010	2.00	-57.0
5	0.010	2.00	-58.0
12	0.010	2.00	-59.5

The cavitation behavior at the runner was also monitored through capturing images and video recording using the high-speed camera for comparison purposes. The air injection could be distinguished by observing the air bubbles at blades side. Figure 48 exhibits a captured image via the high-speed camera of the propeller spinning at 2000 rpm and without aeration. The cavitation bubbles can be observed detaching the tip of the blades and forming a cone-like shape "cavitation cloud" downstream of the runner as indicated in Figure 48. The air injection cases are shown in Figures 49, 50, 51, and 52 representing the 0 psig, 3 psig, 5 psig, and 12 psig A.I. cases respectively. When comparing these figures, it can be noticed that with increasing the air injection pressure more bubbles were observed at the blades side of the runner, in other words; where the air injection ports exist. The cavitation bubbles and the injected air could not be differentiated from looking at these figures only. However, it can be inferred that there is a difference between the no aeration and air injection cases in terms of the quantity of these bubbles as well as the cone-like cavitation cloud mixed with air at the that the downstream of the runner. The size of this cloud is getting bigger as the air pressure was increased in addition to covering most of the runner as seen from the figures. The cavitation behavior and pattern were studied through the image processing and discussed more in the experimental – CFD validation section.
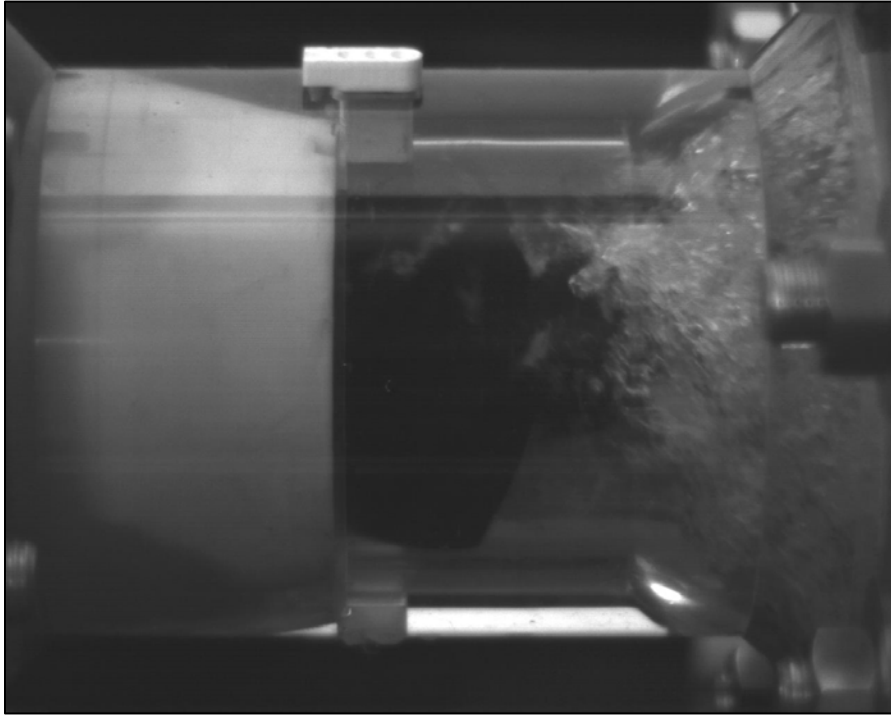
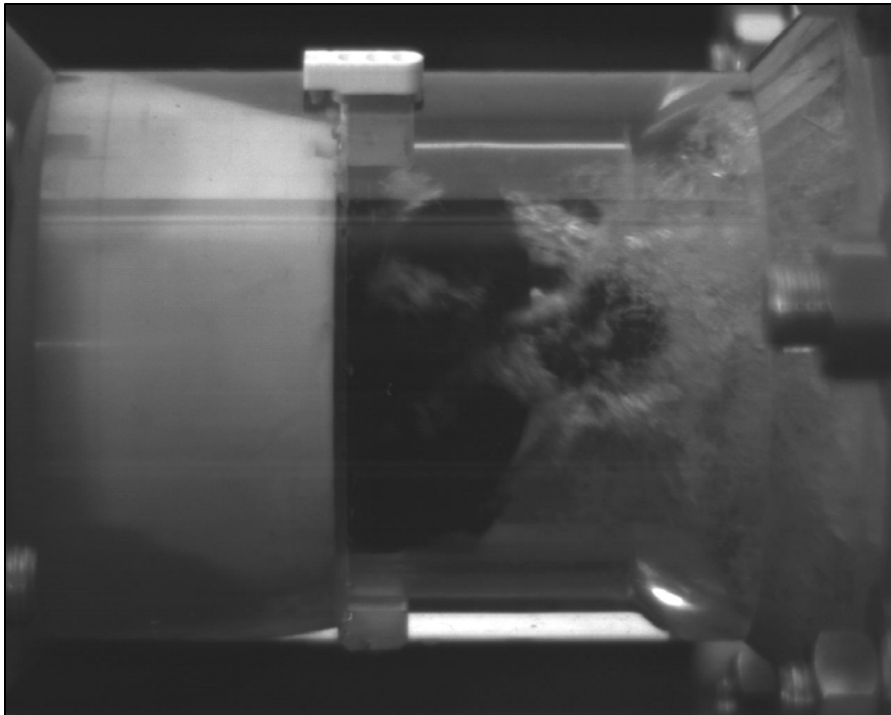Figure 48: Experimental testing image – No air 2000 rpm

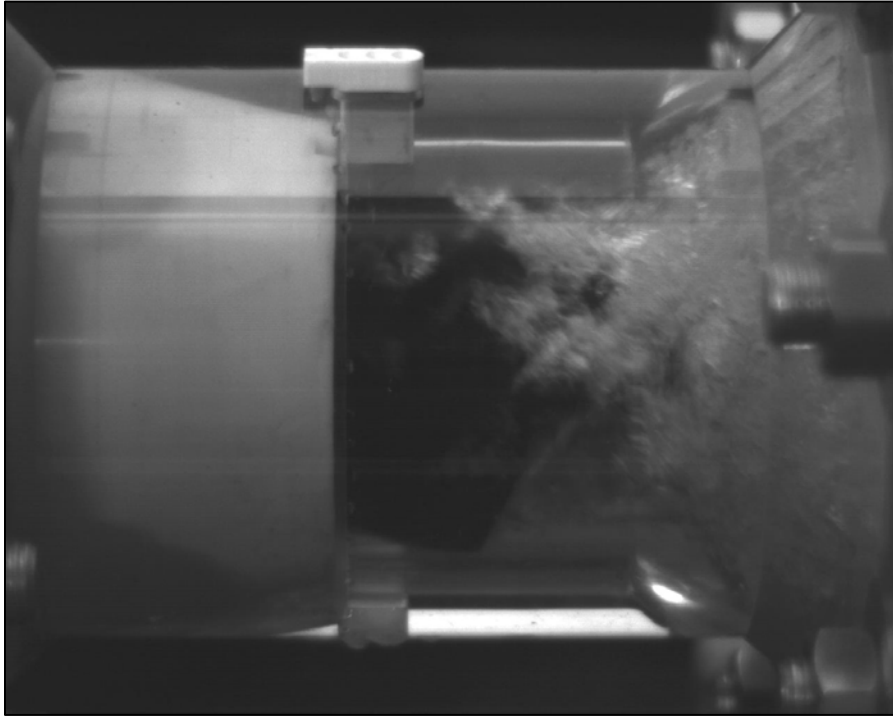Figure 49: Experimental testing image – 0 psig A.I. 2000 rpm

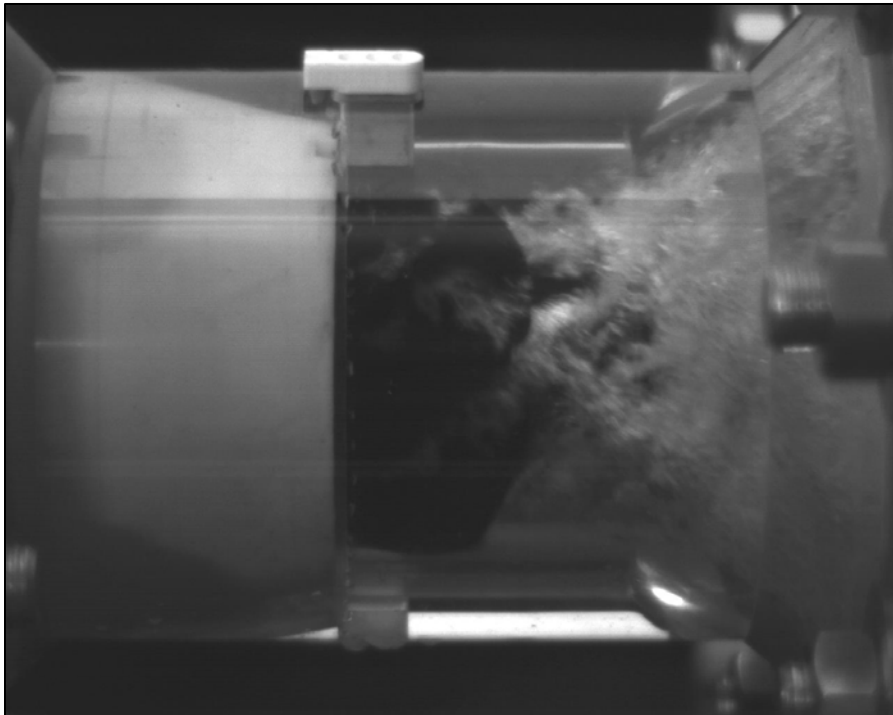Figure 50: Experimental testing image – 3 psig A.I. 2000 rpm

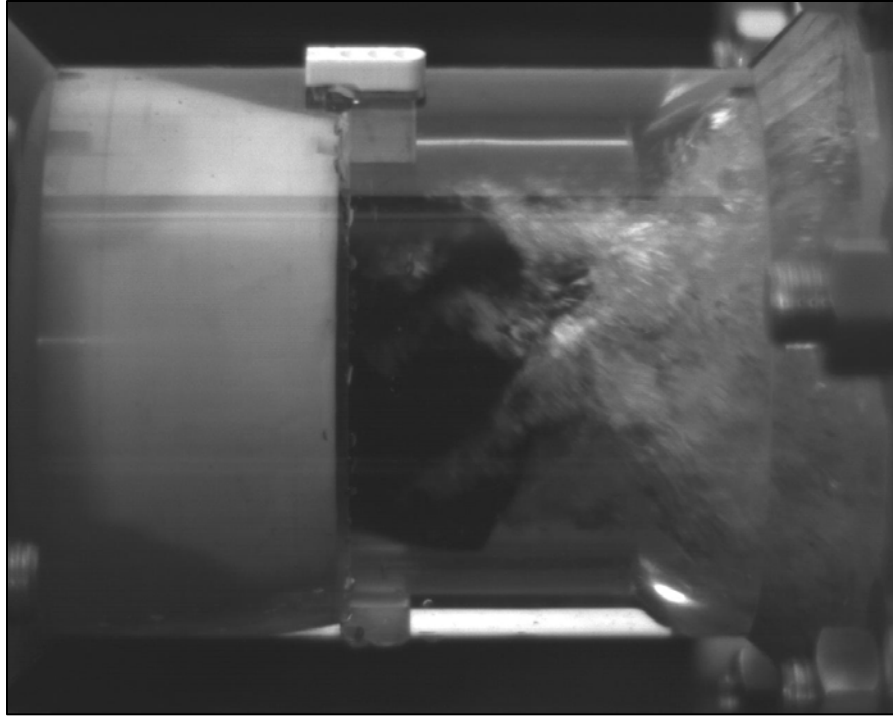Figure 51: Experimental testing image – 5 psig A.I. 2000 rpm

Figure 52: Experimental testing image – 12 psig A.I. 2000 rpm

4.2.3 Propeller Case – 3000 rpm

After testing the propeller at 2000 rpm, the rotational speed was increased to 3000 rpm using the DC motor controller as to investigate the effect of air injection on the power and cavitation behavior at different speeds. The results of the 3000 rpm experimental testing are shown in Table 12. Similar to the first experimental case, the power in the propeller scenario is indicated in negative since it reflects the power consumption. In this case, more power was consumed than in the 2000 rpm case since the rotational speed was increased. The power consumption in the 3000 rpm varied from 197.0 W to 201.0 W whereas 55.0 W to 59.5 W in the 2000 rpm case. The water flow rate and head were increased in the 3000 rpm case to allow for the increase the rotational speed. Moreover, the trend between the two cases was analogous showing an increase in the power consumption as the air injection pressure increased. This leads to a conclusion that the air injection

will affect the power output of the turbine adversely since propellers and turbines have similar

characteristics and exhibit same performance trend.

Table 12: Propeller 3000 rpm case summary of experimental results

Air pressure (psig)	Water Flow Rate (m³/s)	Head (m)	Power (W)
No air	0.0108	2.10	-197.0
0	0.0108	2.10	-198.0
3	0.0108	2.10	-198.5
5	0.0108	2.10	-199.0
12	0.0108	2.10	-201.0

Similar cavitation behavior as the 2000 rpm case was observed in the 3000 rpm rotational

speed case. The cavitation cloud mixed with the air injected downstream of the runner followed

the same pattern in the 2000 rpm rotational speed case. Figures 53 -57 demonstrate the change of

the cavitation pattern, as well as the stream of the air bubbles that observed in the A.I., between

the no aeration, 0 psig, 3 psig, 5 psig, and 12 psig A.I. cases. It was observed that the cavitation

cloud downstream the runner is bigger than in the 2000 rpm cases.
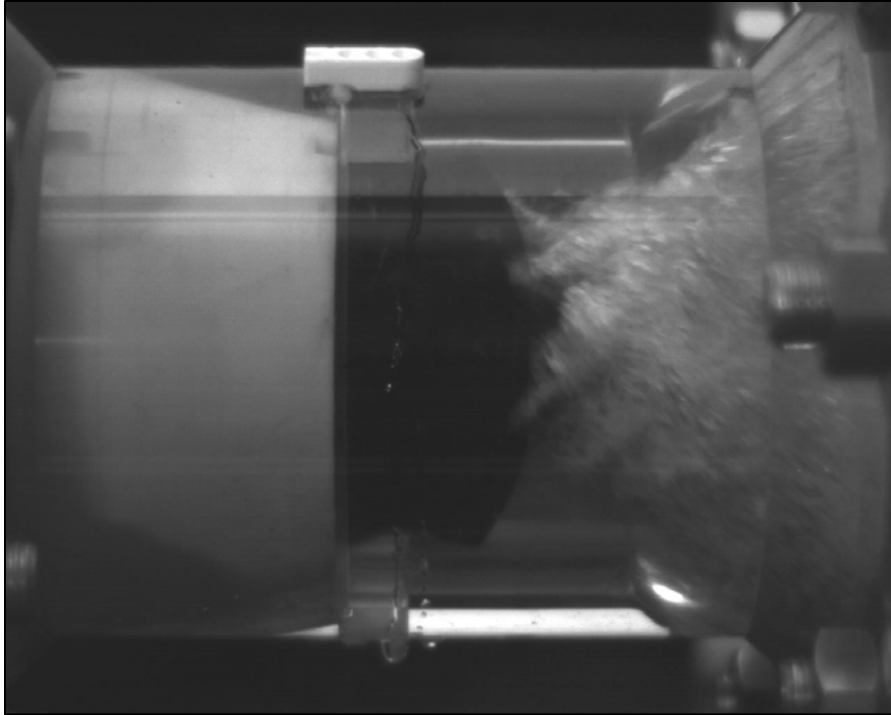
Figure 53: Experimental testing image – No air 3000 rpm
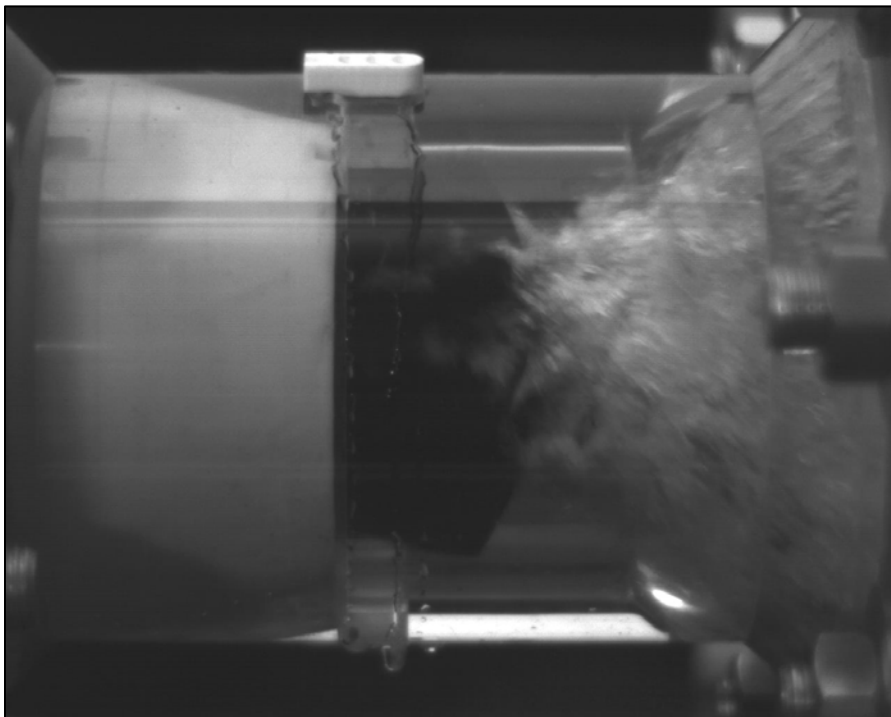

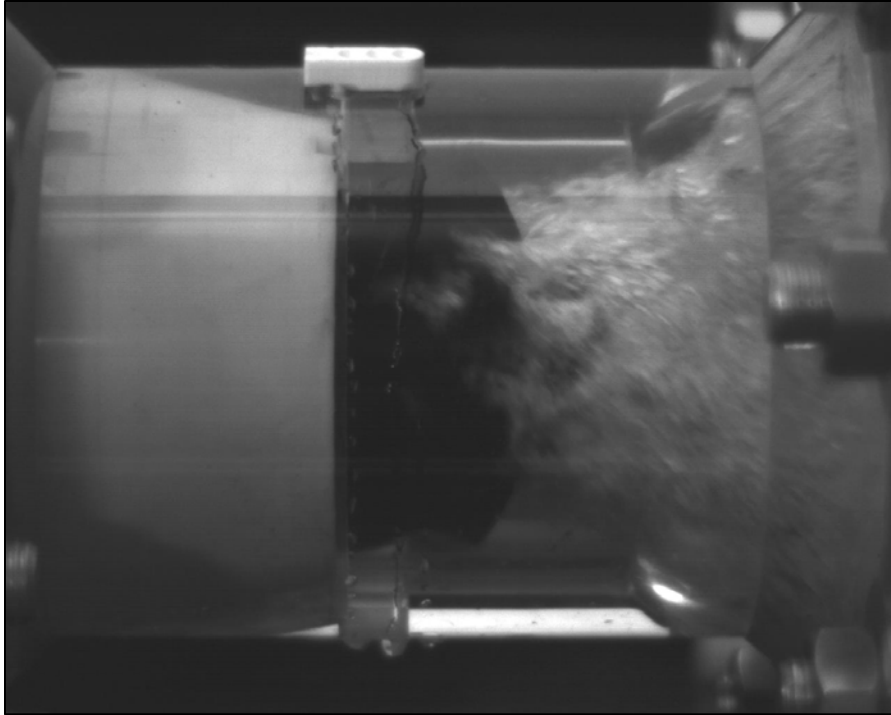Figure 54: Experimental testing image – 0 psig A.I. 3000 rpm

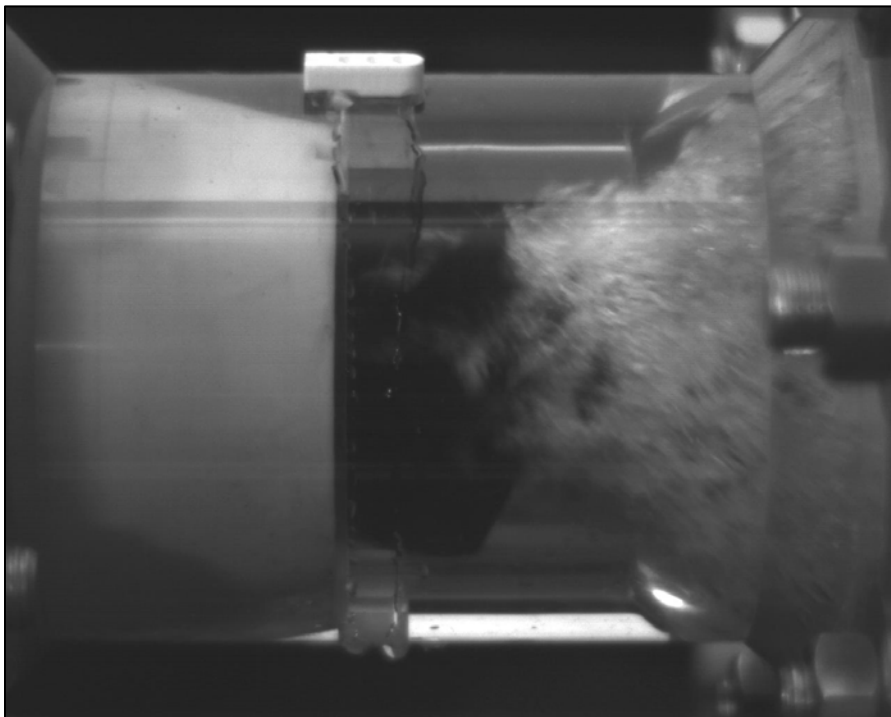Figure 55: Experimental testing image – 3 psig A.I. 3000 rpm

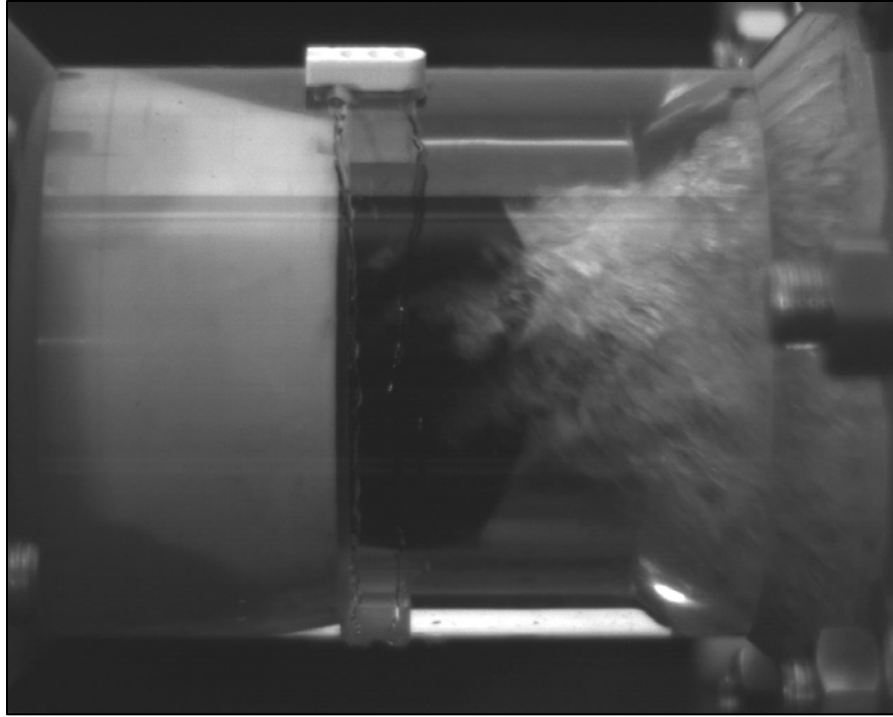Figure 56: Experimental testing image – 5 psig A.I. 3000 rpm

Figure 57: Experimental testing image – 12 psig A.I. 3000 rpm

4.3 CFD – Experimental Validation Results

The results comparison and validation between the CFD and experimental work that was adhered comprised of three parameters: visual validation, CFD simulation results, and image processing. The first case that was investigated is the 2000 rpm no aeration having a water flow rate of 0.010 m³/s in the 0.15 m pipe ahead of the propeller. The images of the experimental testing captured via the high-speed camera were set along the time averaged VVF scenes to compare the cavitation behavior. Figure 58 illustrates an image of the experimental test and a CFD VVF scene of the 2000 rpm case. The cavitation formation in the experimental testing, as shown in Figure 58 (a), started at the blade leading edge and extended towards the succeeding rotor blade before going downstream and merging with the cavitation cloud that formed in similar approach. The CFD VVF

scene, Figure 58 (b), indicated analogous trend of the cavitation formation at the blades and merging with the cavitation cloud downstream as represented in the white colored formation.
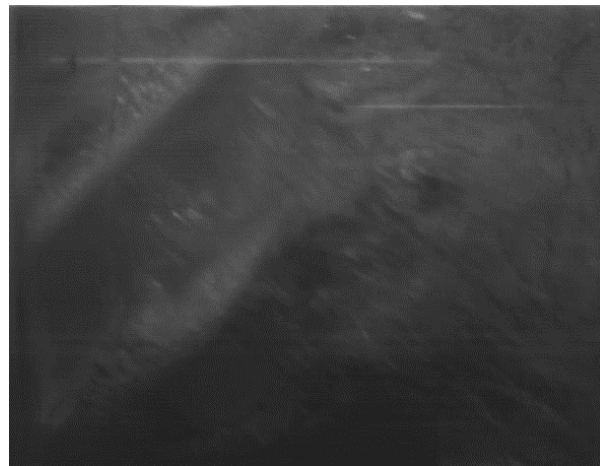
(a)
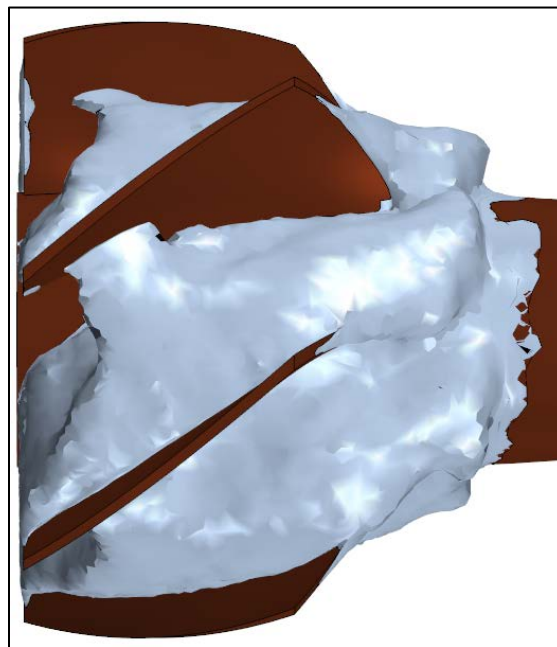
(b)

Figure 58: Visual comparison no aeration 2000 rpm : (a) experimental (b) CFD VVF scene

The power consumed to spin the propeller in the experimental case was 55 W whereas reaching up to 67 W in the CFD simulation. As inferred, the power consumption has similar order of magnitude and showed a deviation of 17.9%.

The last step that was used in the validation of this case is the image processing to estimate the percentage of the cavitation. This process incorporated cropping the CFD and experimental images to include the area between two blades, contrast enhancement, and converting into binary images (0 = black and 1 =white) as well as RGB (red, green, and blue) colors to differentiate the pixels. This process is illustrated in Figure 59 and 60 for the experimental part and CFD VVF scene, respectively.
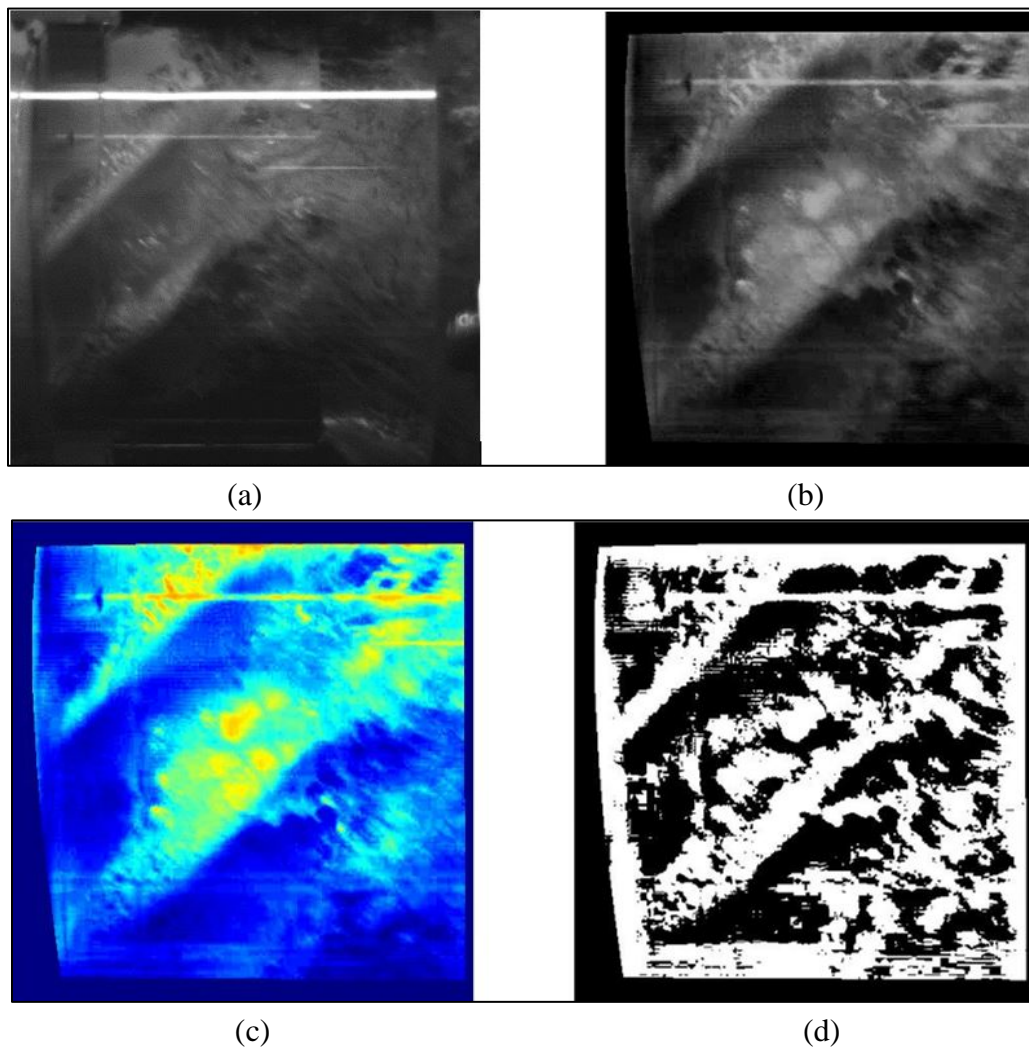

(a)　　　　　　　　　　　　　　　　(b)

(c)　　　　　　　　　　　　　　　　(d)

Figure 59: Experimental image processing: (a) original image, (b) enhanced contrast, (c) RGB converted image, (d) binary converted image
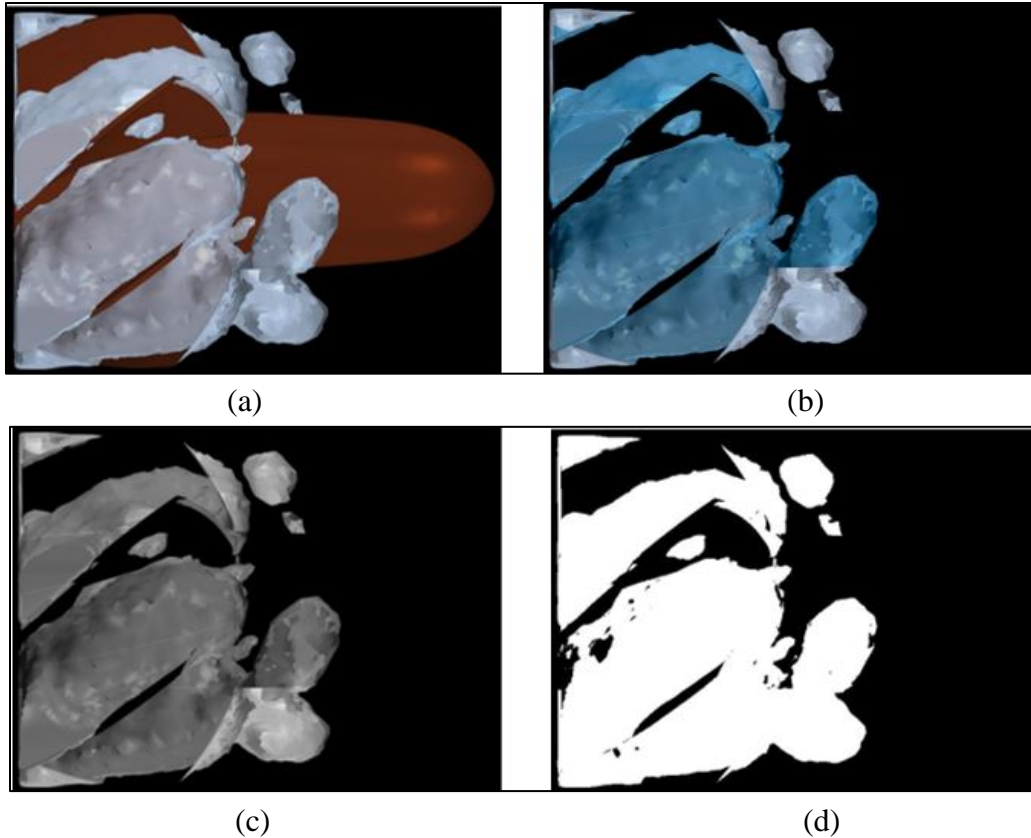
Figure 60: CFD image processing: (a) original image, (b) cropped rotor image, (c) grayscale

converted image, (d) binary converted image

The bright colored areas, shown in Figure 59 (c), indicated the cavitation areas whereas the

dark blue color is the no cavitation zone. The visual indication of this phenomenon led to the

validation that cavitation started at the leading edge of the blade, extended, and then detached from

the blade. The same cavitation behavior was observed in the CFD as shown in grayscale image,

Figure 60 (c). In the CFD case, the cavitation was also generated at the blade leading edge and

detached later as it extended downstream of the runner. The white pixels in the binary image were

added, and then divided on the total number of pixels including the white and black. The ratio

obtained indicated the cavitation area percentage and this procedure was followed in both CFD

and experimental images. The results showed very close cavitation area percentage between the

experimental image, 44%, versus 47% for the CFD scene as shown in Figure 61

(a)   (b)
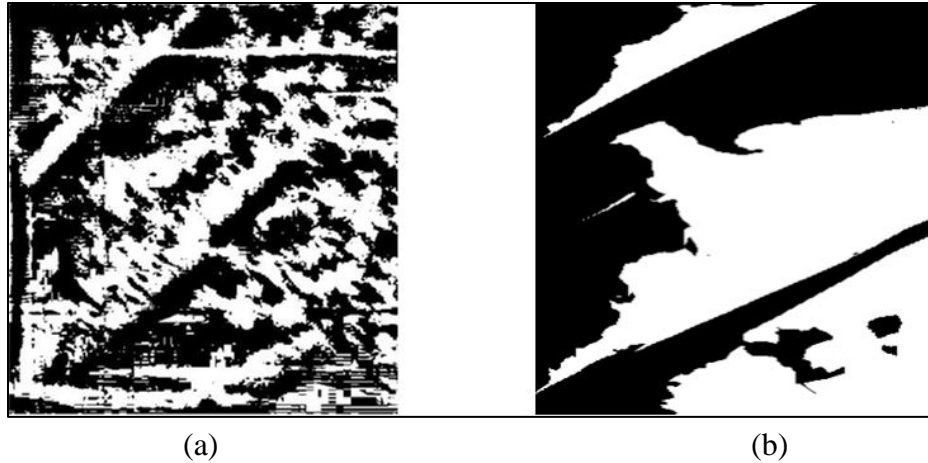
Figure 61: 2000 rpm case image processing – binary images: (a) experimental (b) CFD

The approach detailed previously, was adopted to the 3000 rpm case as well. The water flow rate modeled in the CFD was 0.0108 m³/s in the 0.15 m inlet pipe to simulate the same flow parameters that were achieved in the experimental testing. The power consumed in the experimental part was 197.0 W while the CFD simulation had a power consumption of 220.0 W. As for the cavitation area percentage, the image processing of the CFD scene exhibited 59% whereas the experimental part indicated 56% cavitation area. The image processing of the experimental part and CFD scene for the 3000 rpm case are illustrated in Figure 62.
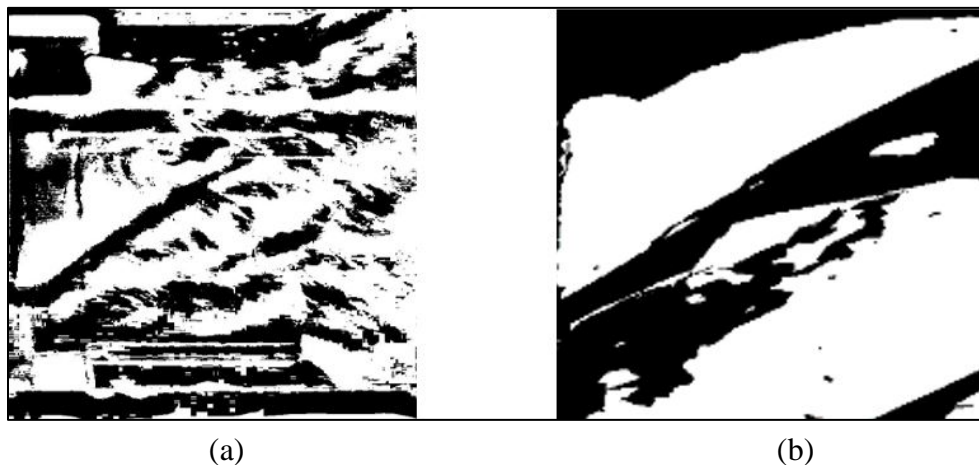

(a)   (b)

Figure 62: 3000 rpm case image processing – binary images: (a) experimental, (b) CFD

5. Conclusions

In this study, a method to treat the cavitation phenomenon in a hydro turbine was introduced. The performance of the turbine and cavitation treatment via air injection were investigated numerically and experimentally. The study was conducted on a micro Kaplan hydro turbine of 0.076 m (3-inch) diameter with a low-head application, not exceeding 2.50 m (8 ft). The turbine geometrical parameters were designed in house having 9 stator blades and 5 rotor blades. The numerical investigations were carried out using CFD modeling software. The experimental setup was built up in the Hydro Turbine Lab at the University of Wisconsin-Milwaukee.

The CFD simulations monitored the power generated through the turbine as well as the VVF scenes to study the cavitation behavior. With five rotational speeds per each case, four cases were simulated including no aeration and three air injection cases at different pressures. The first case was simulated without air injection as to provide a baseline data for the comparison process. Then, air was introduced at 101.3 kPa (0 pisg), 122.0 kPa (3 psig), and 135.8 kPa (5 psig) to examine the effect of injecting air at different pressures. The air was injected via one port at the suction side of each rotor blade close to the leading edge through a port of 3mm diameter and concluding to five ports in total.

The designed turbine was 3-D printed along with other parts, such as the air injection chamber, and were used in building the experimental setup for testing. The experimental setup had two reservoirs; elevated tank up-stream of the turbine and down-stream sink with a circulating pump in between. The turbine was installed in a clear housing to capture the cavitation by a high-speed camera. Air was injected using a compressed air system and introduced to the setup via a specially designed air-tight chamber attached to the exit elbow of the setup. The air was transferred

to the leading edge of the rotor blades through a hollowed stainless-steel shaft and internal channels. The setup was tested as a propeller by using a motor to spin the turbine since cavitation was not induced naturally due to some setup limitations. The power consumption and the images captured by the high-speed camera were used in the validation and comparison process.

The validation and comparison were accomplished through three steps: visual validation, CFD simulation results, and image processing. Another CFD models were conducted to simulate the experimental propeller case. The VVF scenes and high-speed camera images were compared and validated, visually, the cavitation behavior and pattern. The power consumption measured during the experimental runs were matching in terms of order of magnitude to the values obtained numerically, however showed acceptable deviations. The image processing confirmed the percentages of the cavitation area, numerically and experimentally, with almost matching values.

As a result, the following can be concluded for the turbine case:

1- The air injection showed an increase in the absolute pressure in the system offsetting some zones pressure above the water vapor pressure.

2- Air injection at 0 psig showed an average blades VVF reduction of 25.3%, hub VVF reduced by 65.1%, and the power generated decreased by 11.4% when compared to no aeration case.

3- Air injection at 3 psig showed an average blades VVF reduction of 33.6%, hub VVF reduced by 73.1%, and the power generated decreased by 9.5% when compared to no aeration case.

4- Air injection at 5 psig showed an average blades VVF reduction of 49.7%, hub VVF reduced by 90.6%, and the power generated decreased by 6.6% when compared to no aeration case.

5- The cavitation was further reduced while increasing the air injection pressure.

6- The cavitation reduction was substantial and reached to 50% in some cases.

7- The turbine power generation was adversely affected by the air injection.

8- The 0 psig air injection case had the highest power reduction.

9- The reduction in the power generated were mitigated as the air injection pressure increased.

10- The air injection exhibited an effective method in the mitigation and treatment of the cavitation phenomenon.

Future Work Recommendations

The work that was completed during this study is promising and can lead to a breakthrough in the cavitation treatment technologies, extending the lifespan of the hydro turbines, and enhancing their performance over time. Additionally, due to the complexity of the fluid dynamics in such systems that involve phase changing and multiple fluids in a rotational domain few studies related to air injection treatment had been completed in the past. Thus, more research can be conducted to prove the outcomes of this study and lead to a better understanding of the air injection effect on the cavitation phenomenon in hydro turbines. Therefore, the following can be investigated in the future on the same setup to expand on this study:

1. Examine the effect of changing the air injection ports size and location.

2. Introduce the air through the blade walls by increasing the walls thickness and incorporate channels in the blades.

3. Expand the experimental setup by extending the head and increasing the tanks volume to enable running it as a turbine case.

References

[1]   Renewables 2018 Global Status Report, REN21, Paris, France.

[2]   World Energy Resources: Hydropower 2016, World Energy Council.

[3]   U.S. Energy Information Administration (EIA) Report: Monthly Energy Review, March 2018, U.S. Department of Energy, Washington, DC, USA.

[4]   World Energy Resources 2016 Report, World Energy Council.

[5]   U.S. Geological Survey, December 2016, U.S. Department of the Interior, USA. URL: http://water.usgs.gov/edu/hybiggest.html

[6]   2014 Hydropower Market Report, April 2015, Oak Ridge National Laboratory U.S. Department of Energy, TN, USA.

[7]   Applegate Group, Inc., 2010, "Section 1: Low Head Turbines", Applegate Group official website, URL: http://www.applegategroup.com/node/176

[8]   Glenn Machado, Oct. 2009, "Polymeric Solution for Pumps Suffering from Cavitation", Pumps and Systems, Cahaba Media Group.

[9]   Brennen, C. E., 2013, Cavitation and bubble dynamics, Cambridge University Press, UK.

[10] Nelik L., 2016, "Cavitation vs. Air Entrainment" https://www.pumpsandsystems.com/pumps/january-2016-cavitation-vs-air-entrainment

[11] Yakushiji, R., 2009. Mechanism of tip vortex cavitation suppression by polymer and water injection (Doctoral dissertation, University of Michigan).

[12] Kumar P., Saini R.P., 2010, " Study of Cavitation in Hydro Turbines – A Review", Renewable and Sustainable Energy Reviews 14 374-383.

[13] Kubota A., Kato H., Yamaguchi H., 1992, "A new modelling of cavitating flows—a numerical study of unsteady cavitation on a hydrofoil section", Journal of Fluid Mechanics, 59–96.

[14] Bark G., Van Berlekom W.B., 1978, "Experimental investigations of cavitation noise", Proceedings of 12th ONR Symposium on Naval Hydrodynamics, 470-493.

[15] Amano, R.S., Lequesne, B., and Millevolte, J., March 2017, "Very Low-Head Hydro Turbine Research," US Department of Energy, EERE Grant, Grant Number: DE-FOA-0001417.

[16] Kermeen R.W., 1956, "Water tunnel tests of NACA 4412 and Walchner Profile 7 hydrofoils in non-cavitating and cavitating flows", Calif. Inst. of Tech. Hydro. Lab. Rep. 47-5.

[17] Kjolle, A., 2001, Hydropower in Norway, Trondheim, Norway.

[18] Duncan Jr. W., 2000, "Turbine manual. Facilities Instructions, Standards, & Technique".

[19] Escalera X., Egusquiza E., Farhat M., Avellan F., Coussirat M., 2006, "Detection of Cavitation in Hydraulic Turbines", Mechanical Systems and Signal Processing 20, 983–1007.

[20] Bajic B., 2003, "Methods for Vibro-Acoustic Diagnostics of Turbine Cavitation", Journal of Hydraulic Research 41, 87–96.

[21] Grekula M, Bark G., "Experimental study of cavitation in a Kaplan model turbine" CAV2001:session B9.004.

[22] Xian-wu L., Bin JL., Tsujimoto Y., 2016, "A review of cavitation in hydraulic machinery", Journal of Hydrodynamics; 28(3), 335–358.

[23] Arndt R. E., Ellis C. R., Paul S., Sep. 1995, "Preliminary Investigation of the Use of Air Injection to Mitigate Cavitation Erosion", Journal of Fluids Engineering; 117(3), 498-504.

[24] Zhi-yong D., 2006, "Cavitation Control by Aeration and Its Compressible characteristics", Journal of Hydrodynamics, Ser.B, 18(4), 499-504

[25] Tomov P., Khelladi S., Ravelet F., Sarraf C., Bakir F., and Vertenoeuil P., 2016, "Experimental Study of Aerated Cavitation in a Horizontal Venturi Nozzle", Experimental Thermal and Fluid Science, 70, pp.85-95.

[26] Rivetti A., Angulo M., Lucino C., and Liscia S., 2011, "Computational Fluid Dynamics and Heat Transfer Emerging Topics", 9th International Symposium on Cavitation (CAV2015), Journal of Physics: Conference Series 656.

[27] Siemens PLM Software STAR CCM+ brochure. Available online at: http://mdx.plm.automation.siemens.com/sites/all/themes/basic/assets/downloads/STAR-CCM+%20v11%20brochure%202016.pdf

[28] Amano R.S., Sunden B., 2015, "Pressurized Air Injection in an Axial Hydro-Turbine Model for the Mitigation of Tip Leakage Cavitation", WIT Press, UK.

[29] Boersma, B.J. and Lele, S.K., 1999, "Large Eddy Simulation of Compressible Turbulent Jets", Center for Turbulence Research, Annual Research Briefs, pp. 365-377.

[30] Leonard, A., 1975, "Energy Cascade in Large-Eddy Simulations of Turbulent Fluid Flows.", Advances in geophysics 18 (1975): 237-248.

[31] Knight, D., Zhou, G., Okong'o, N. and Shukla, V., 1997, August, Large Eddy Simulation of Compressible Flows Using Unstructured Grids, In First AFOSR International Conference on DNS/LES.

[32] Schmitt, F.G., 2007, "About Boussinesq's Turbulent Viscosity Hypothesis: Historical Remarks and a Direct Evaluation of its Validity", Comptes Rendus Mécanique, 335(9-10), pp.617-627.

[33] Ducros, F., Nicoud, F. and Poinsot, T., 1998, "Wall-Adapting Local Eddy-Viscosity Models for Simulations in Complex Geometries", Numerical Methods for Fluid Dynamics VI, pp.293-299

[34] Nicoud, F., and Ducros, F., 1999, "Subgrid-Scale Stress Modelling Based on the Square of the Velocity Gradient Tensor," Flow, Turbulence and Combustion, 62, pp. 183-200

[35] T.Kajishima, 1999, Computational simulations of turbulent flow, Youkendou, Tokyo, Japan.

[36] Noh, W.F. and Woodward, P., 1976, "SLIC (Simple Line Interface Calculation)", Proceedings of the Fifth International Conference on Numerical Methods in Fluid Dynamics, Twente University, Enschede, NL, pp. 330-340. Springer Berlin Heidelberg.

[37] Hirt, C.W. and Nichols, B.D., 1981, "Volume of Fluid (VOF) Method for the Dynamics of Free Boundaries", Journal of computational physics, 39(1), pp.201-225.

[38] Schnerr, G.H. and Sauer, J., 2001, May, Physical and numerical modeling of unsteady cavitation dynamics. In Fourth international conference on multiphase flow, New Orleans, USA, Vol. 1.

[39] Stephen B. Pope, 2000, "Turbulent Flows", Cambridge University Press, NY, USA.

[40] B. E. Launder, D. B. Spalding, 1972, "Lectures in Mathematical Models of Turbulence", Academic Press, London UK.

[41] Pletcher R. H., Tannehill J. C., and Anderson D. A., 2013, "Computational Fluid Mechanics and Heat Transfer", Third Edition, CRC Press, FL, USA.

[42] Colorfabb NGen filament; in particular, Eastman Amphora 3D Polymer AM3300; http://colorfabb.com/files/AmphoraAM3300-TDS.pdf.

[43] Ultimaker 2+ 3D printer specification. Available online at: https://ultimaker.com/en/products/ultimaker-2-plus

[44] FASTCAM Mini UX50 data sheet, available online at: https://photron.com/mini-ux/

[45] Badger-Meter electromagnetic flow-meter, Model M-2000 M-Series Mag meter. Available online at: https://www.instrumart.com/assets/Badger-M2000_manual.pdf

[46] Magtrol torque-meter. Available online at:
http://www.magtrol.com/manuals/tm300manual.pdf

[47] Magtrol torque-display. Available online at:
https://www.magtrol.com/wp-content/uploads/3411.pdf

[48] Icon Health and Fitness DC motor. Available online at:
https://www.surpluscenter.com/Catalog/Catalog291-164.pdf

[49] NEMA 4X/IP65 DC motor control. Available online at:
http://acim.nidec.com/drives/kbelectronics/products/variable-speed-dc-drives/dc-drives-nema-4

[50] ATM 10 HP pump. Available online at:
http://amtpumps.com/site/wp-content/uploads/2017/01/STE-15-16.pdf

[51] ABB ACS310 VSD. Available online at:
https://library.e.abb.com/public/f54878880ad34bbd855ee0008d6d13a6/3AUA0000159910_REVG.pdf